photonics

MDPI

Article

Photon Blockade in a Laguerre–Gaussian Optorotational System with Cross-Kerr Nonlinearity

Ke-Dong Liu, Tai-Shuang Yin * and Aixi Chen

Zhejiang Key Laboratory of Quantum State Control and Optical Field Manipulation, Department of Physics, Zhejiang Sci-Tech University, Hangzhou 310018, China; 2023210104010@mails.zstu.edu.cn (K.-D.L.); aixichen@zstu.edu.cn (A.C.)
* Correspondence: taishuangyin@zstu.edu.cn

Abstract

We explore the generation of photon blockade effect in a Laguerre–Gaussian optorotational system where a Gaussian beam exchanges orbital angular momentum with a rotating spiral phase mirror. In addition to the typical optorotational coupling, we consider the existence of cross-Kerr nonlinearity between the cavity mode and the rotating mirror. We investigate the statistical characteristics of photons by numerically and analytically calculating the second-order correlation function. In particular, we find that the antibunching effect of photons is dominated by the cooperative operation between the optorotational coupling and the cross-Kerr coupling instead of any individual part. The optimal single photon blockade can be achieved in a moderate coupling regime and enhanced due to the presence of cross-Kerr nonlinearity. The dependence of photon blockade effect on the different system parameters is discussed in detail. Our work provides an alternative way to manipulate the photon quantum behaviors in Laguerre–Gaussian optorotational systems, which may find potential applications in quantum information processing and optical communication utilizing the optical orbital angular momentum.

Keywords: photon blockade; Laguerre–Gaussian optorotational system; cross-Kerr nonlinearity; orbital angular momentum

1. Introduction

Exploring the quantum behaviors of systems at a macroscopic scale is of fundamental importance for revealing the quantum–classical boundary as well as developing quantum-enabled technologies in quantum information processing and quantum measurement [1–5]. In the last decades, significant advances in micro- and nanomechanical fabricating technologies and experimental techniques have been made, which allow the controllable generation and manipulation of nonclassical phenomena [6,7]. For example, considerable achievements have been made including cooling the mechanical modes to their quantum ground state [8–11], the generation of squeezed light and quantum entanglement [12,13]. Note that one of the important quantum effects is photon blockade, which could be induced by a large optical nonlinearity [14,15]. Photon blockade is a paradigmatic effect in which the excitation of a single photon prevents the subsequent absorption of additional photons, yielding sub-Poissonian photon statistics and an antibunching effect [16]. Beyond its fundamental significance, the photon blockade effect offers a promising route to the engineering of new single-photon quantum devices such as single-photon transistors [17],

Received: 6 July 2026
Revised: 26 July 2026
Accepted: 29 July 2026
Published: 30 July 2026

single-photon routers [18–21] and single-photon switches [22], which are key resources for quantum networks and photonic quantum information [23–25].

As a typical effect, photon blockade has attracted considerable attention and has been extensively studied in many platforms, including cavity optomechanical systems [26–28], cavity quantum electrodynamics (QED) systems [16] and other hybrid quantum systems [24]. The achievement of this quantum effect generally originates from two different physical mechanisms. One mechanism is based on strong optical nonlinearity, which can induce the energy-level anharmonicity of coupled systems [14,29–31]. Thus, due to the frequency detuning, the probability of multi-photon transition is dramatically suppressed in the case of single-photon resonant excitation. Experimental research has demonstrated this quantum effect in a strongly coupled optical cavity containing one trapped atom [16]. In contrast, the other physical mechanism relaxes the requirement for the strong system nonlinearity, which ultimately allows the generation of photon blockade even though the intrinsic nonlinearity is in the weak coupling regime. Many theoretical works investigate this quantum effect with weak nonlinearities [32,33]. Essentially, this phenomenon is caused by the quantum destructive interference between different excitation pathways [34–36]. This unconventional photon blockade effect has also been experimentally observed in a quantum dot cavity QED system [37] and a superconducting circuit system involving two coupled resonators for microwave photons [38].

Note that in recent years, a Laguerre–Gaussian (LG) optorotational system as an emerging and powerful platform is proposed. The LG optorotational system consists of two spiral phase elements [39,40]. One of them is an input coupler, which is fixed and partially transparent. The other spiral phase element is a movable perfectly reflecting rear mirror, which can rotate about the cavity axis. Different from the typical radiation pressure coupling between a mechanical oscillator and an optical cavity via the exchange of linear momentum, the LG optorotational system explores the optorotational coupling due to the transfer of the orbital angular momentum [41]. Specifically, the LG beam carries an orbital angular momentum of $\hbar l$ per photon along its propagation direction, where l is an integer and represents the topological charge value [42,43]. The spiral phase elements can be designed to modify the azimuthal structure of laser beams, thus changing the topological charge value either via reflection or transmission. As a result, the LG cavity mode is coupled to the rotating rear mirror via radiation torques. In a typical configuration employing spiral phase elements, the cavity mode acquires an orbital angular momentum of $\pm 2\ell$, which can be transferred to a rotating end mirror about the cavity axis [42]. Owing to this unique coupling mechanism, LG optorotational systems have been shown to support a variety of fascinating phenomena, including cooling the rotational motion of a mirror [42,44], the generation of second-order sideband effect [45] and sum-sideband effect [46], optomechanical-induced transparency [47] and quantum entanglement between different modes [48–50]. Note that most existing studies about LG optorotational systems mainly focus on the strong driven regime, where the system dynamics are linearized around a classical steady state. However, to the best of our knowledge, the genuinely nonlinear quantum effects at the single-photon level, especially those related to photon blockade, remain comparatively less explored. This makes the LG cavity a compelling platform for investigating how the nonlinear coupling reshapes the photon statistics in the quantum regime. In conventional analyses of LG optomechanical systems, the discussion is often restricted to situations where only intrinsic optorotational coupling exists. Due to the fact that photon blockade is essentially determined by the nonlinear displacement of the system energy spectrum, additional nonlinear interactions can be introduced to more effectively regulate nonclassical behaviors of photons, such as the introduction of cross-Kerr nonlinearity [51–54]. Cross-Kerr nonlinearity directly correlates the photons and phonons, which can significantly alter the spectral structure and photon statistical properties of the system [55,56].

The typical optical Kerr effect refers to the change in the refractive index of a nonlinear medium if a signal wave is incident on this medium [57,58]. Thus a probe wave propagating through the medium experiences a phase shift, which is proportional to the intensity of the signal wave. The cross-Kerr nonlinear coupling between an optical cavity and the mechanical resonator originates from the change in the refractive index associated with the optical field, which depends on the phonon number in the mechanical resonator. This cross-Kerr-type coupling can be engineered as effective interactions in the context of optomechanical platforms [59,60]. It has been theoretically shown that the cross-Kerr coupling between a mechanical resonator and a microwave cavity can be induced via the Josephson effect [55]. In particular, this coupling has been experimentally demonstrated by introducing a quantum two-level system (qubit) [61]. The photon–phonon cross-Kerr nonlinearity can be further enhanced by additional nonlinear driving or circuit-based nonlinear elements. For example, two-photon driving has been proposed to enhance photon–phonon cross-Kerr nonlinearities [62], and single-photon cross-Kerr nonlinearities can be exponentially enhanced in quantum optomechanics [63]. Moreover, the Josephson capacitance of a Cooper-pair box can be used to enhance optomechanical coupling and Kerr nonlinearity [64]. In addition to qubit-mediated optomechanical implementations, cross-Kerr nonlinearities have also been observed in other quantum platforms, such as cold Rydberg gases [65] and ferrimagnetic crystals [66]. Furthermore, recent studies of Laguerre–Gaussian cavity optorotational systems have exploited this effective cross-Kerr interaction between the LG cavity field and the rotational mechanical mode to enhance the steady-state entanglement and the cooling of a rotating mirror [44,56,67].

Motivated by the above mentioned works, here we explore the controllable photon statistics and the generation of photon blockade effect in a LG optorotational system containing cross-Kerr nonlinearity. By combining analytical and numerical approaches, we examine how the optorotational coupling and cross-Kerr nonlinear coupling modify the effective detuning, the energy-level anharmonicity, and the photon statistical properties of the system. The results show that the photon antibunching effect can be significantly enhanced in a moderate coupling regime. However, either excessively large optorotational coupling or cross-Kerr coupling cannot further enhance the photon blockade. Instead, it may drive the system toward phonon-assisted two-photon resonances that degrade photon blockade. It means that the achievement of the optimal single-photon blockade requires the competitive and cooperative operation between the optorotational interaction and cross-Kerr nonlinear interaction. In addition, we also analyze in detail the influence of system parameters, e.g., the topological charge value, the mass and the radius of the rotating mirror and the environmental temperature on the photon blockade effect. These results provide useful insight into nonlinear quantum statistical effects in LG cavities and offer a alternative proposal for the controllable generation of nonclassical LG light.

Note that most of the research on the photon blockade effect in conventional optomechanical systems exploit the radiation pressure coupling via the exchange of linear momentum between the photons in the cavity and a mechanical resonator, while the LG optorotational systems employ the optorotational coupling through the transfer of the orbital angular momentum (OAM) of light between a LG cavity mode and a spiral phase mirror. These two physical mechanisms for yielding the photon blockade are fundamentally different. In other words, our work provides an alternative OAM-based approach for exploring the single-photon quantum effect. In addition, the technological advances allow the generation of spiral phase mirrors with high precision and low mass as well as high topological charge value [68]. Since the single-photon optorotational coupling is associated with the optical topological charge l, the mass M and the radius R of the rotating mirror, the statistical characteristics of photons in the present scheme can be controllable by adjusting system parameters. Furthermore, the present scheme reveals an optimal parameter window to generate the quantum effect at the level of single photon in a LG cavity with the moderate optorotational coupling and the cross-Kerr coupling. Therefore, our work provides a promising route for manipulating the single-photon quantum effect arising from the optorotational coupling. It may inspire the exploration towards the potential applications based on LG modes and the orbital angular momentum of light fields.

This paper is organized as follows: In Section 2 we describe the Laguerre–Gaussian optorotational system with cross-Kerr nonlinearity and derive the total Hamiltonian. In Section 3 we demonstrate the controllable photon statistics by analytically and numerically calculating the second-order correlation function. In addition, we discuss in detail the influence of different system parameters on the photon blockade effect, including the optorotational coupling strength, the cross-Kerr coupling strength, the topological charge value, the mass and the radius of the rotating mirror and the environmental temperature. In Section 4, we compare our results with representative studies and discuss their experimental relevance and extension to the LG optorotational platform. Finally, the conclusions are presented in Section 5.

2. Theoretical Model

We consider a Laguerre–Gaussian (LG) optorotational system containing cross-Kerr nonlinearity. As shown in Figure 1, the LG optorotational cavity consists of a fixed partially transparent input coupler and a movable perfectly reflecting rear mirror, which are both spiral phase elements. When a Gaussian beam is incident on the cavity, the input coupler can be designed to remove a fixed topological charge $2l$ from the beam upon reflection from either side. However, the topological charge of the transmitted beam passing through the input coupler remains unchanged. Differently, the structure of the rear mirror causes the beam to add a topological charge $2l$ during reflection. Due to the transfer of orbital angular momentum, the Laguerre–Gaussian optical field interacts with the rear mirror. The rear mirror rotates around the z axis of the cavity, which results in angular displacement ϕ from the equilibrium position ($\phi_0 = 0$). In addition, we consider a quantum two-level system that exists on the rear mirror, which induces a cross-Kerr nonlinear coupling between the LG cavity and the rotating mirror. Then, the Hamiltonian of the Laguerre–Gaussian optorotational system with cross-Kerr nonlinearity reads

$$H_{\text{op}} = \hbar\omega_c a^\dagger a + \frac{L_z^2}{2I} + \frac{1}{2} I\omega_m^2 \phi^2 - \hbar g_\phi \phi a^\dagger a + H_{\text{ck}}, \tag{1}$$

where a ($a^\dagger$) is the annihilation (creation) operator of the cavity mode and L_z and ϕ represent the angular momentum and angular displacement of the rear mirror that satisfies the commutation relationship $[\phi, L_z] = i\hbar$. The first term in Equation (1) represents the Hamiltonian of the LG cavity field with frequency ω_c. The next two terms are the Hamiltonian of the rotating mirror with angular frequency ω_m. Note that the rotating mirror can be treated as a torsional pendulum of mass M and radius R and thus the moment of inertia is $I = \frac{1}{2}MR^2$. The fourth term describes the optorotational coupling with the coupling parameter g_ϕ. The last term represents the cross-Kerr nonlinear coupling between the cavity mode and the rotating mirror. Here we introduce b ($b^\dagger$) as the annihilation (creation) operator of the rear mirror, which is defined as $\phi = \sqrt{\hbar/2I\omega_m}(b + b^\dagger)$, $L_z = -i\sqrt{\hbar I\omega_m/2}(b - b^\dagger)$. Then the system Hamiltonian can be expressed as

$$H = \omega_c a^\dagger a + \omega_m b^\dagger b - g_0 a^\dagger a(b + b^\dagger) - g_{\text{ck}} a^\dagger a b^\dagger b, \tag{2}$$

with $g_0 = g_\phi\sqrt{\hbar/2I\omega_m}$ being the single-photon optorotational coupling strength and $g_{\rm ck}$ the cavity–mirror cross-Kerr nonlinear strength. Throughout the Hamiltonian formulation and the dynamical calculations, we set $\hbar = 1$, so that energies, Hamiltonians, and coupling parameters are expressed in angular-frequency units. However, $\hbar$ is retained explicitly in dimensional physical relations, including the quantization relations for the angular displacement and angular momentum, the definition of the single-photon optorotational coupling strength, and the thermal phonon occupation number, in order to preserve dimensional consistency.

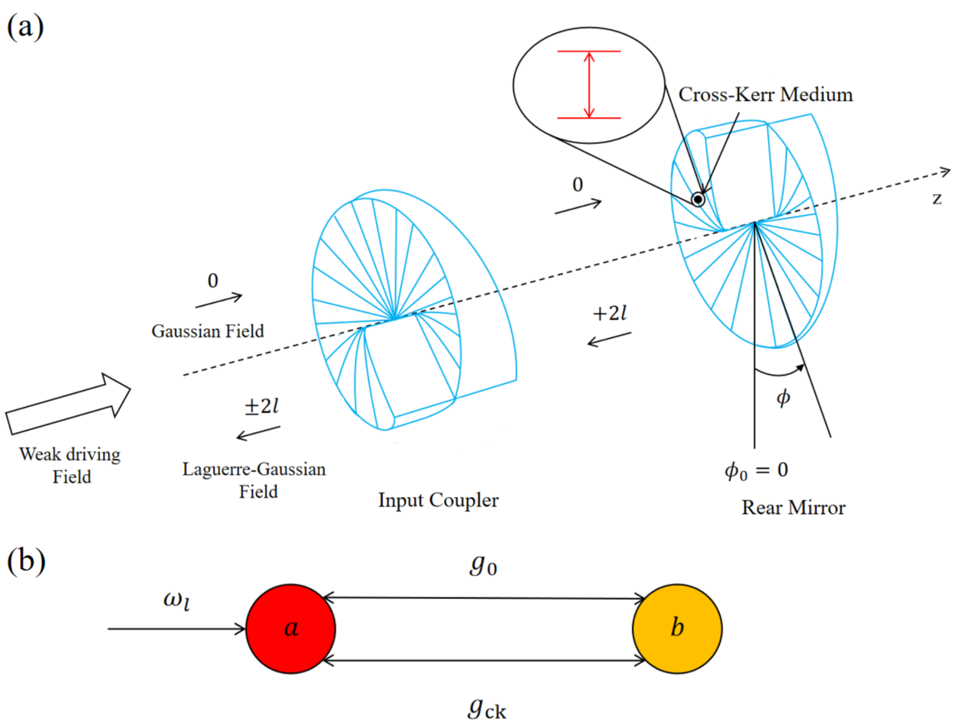

Figure 1. (**a**) The model diagram consists of two spiral phase mirrors to form a Laguerre–Gaussian optorotational system. The Gaussian light with zero orbital angular momentum (OAM) is incident into the cavity through the input coupling mirror and propagates back and forth between the two mirrors. The rear mirror can rotate in the direction of the cavity axis z and its angular displacement is ϕ (equilibrium position $\phi_0 = 0$). The optical field and the rotating rear mirror generate the optorotational coupling by exchanging the orbital angular momentum. The cross-Kerr medium (red two-level image) is introduced near the rear mirror to realize the cross-Kerr coupling between the light field and the rotating mirror. (**b**) Equivalent schematic diagram of the model for two modes: the cavity mode a is driven by a weak driving field with frequency ω_l, and interacts with the rotating mechanical mode b through the optorotational coupling intensity g_0 and the cross-Kerr coupling strength $g_{\rm ck}$.

To solve the eigensystem corresponding to the Hamiltonian H, we introduce a displacement operator $D(\lambda) = \exp[\lambda(b^\dagger - b)]$ with $\lambda = g_0 a^\dagger a/(\omega_m - g_{\rm ck} a^\dagger a)$ and apply it to the Hamiltonian via a unitary transformation $H' = D^\dagger H D$. Then one can obtain the system eigenvalues $E_{n,m} = n\omega_c + (\omega_m - n g_{\rm ck})m - \delta^{(n)}$, where n, m are photon numbers and phonon numbers, respectively, and $\delta^{(n)} = g_0^2 n^2/(\omega_m - n g_{\rm ck})$. And the corresponding eigenstates are $|n\rangle_a|\tilde{m}(n)\rangle_b$, where $|n\rangle_a$ are photon number states of the cavity mode a. For the case of n photons, the mechanical states are the n-photon displaced number states $|\tilde{m}(n)\rangle_b = D(\lambda^{(n)})|m\rangle_b$ for mode b where $\lambda^{(n)} = n g_0/(\omega_m - n g_{\rm ck})$. The detailed derivation of how the system Hamiltonian is diagonalized is presented in the Appendix A. Due to the cavity–mirror optorotational coupling and cross-Kerr coupling, the equilibrium position of the rear mirror is displaced by an amount $\lambda^{(n)}$. Importantly, the effective optical nonlinearity is induced, i.e., $\delta^{(n)}$, which could lead to the generation of photon blockade effect. Note that in the absence of cross-Kerr nonlinearity, i.e., $g_{\mathrm{ck}} = 0$, the system Hamiltonian is reduced to a standard optomechanical Hamiltonian and the Kerr nonlinearity is obtained $\delta^{(n)} = g_0^2 n^2/\omega_m$. However, in the presence of cross-Kerr nonlinearity, i.e., $g_{\mathrm{ck}} \neq 0$, the induced optical nonlinearity $\delta^{(n)}$ is not proportional to the photon number n.

To observe the photon blockade effect, a weak driving field with frequency ω_l and strength Ω is applied to the LG cavity from the input coupler and the Hamiltonian is $H_{\mathrm{p}} = i\Omega(a^\dagger e^{-i\omega_l t} - a e^{i\omega_l t})$. In a frame rotating with frequency ω_l for the optical mode, the total Hamiltonian of the system is transformed as

$$H_{\mathrm{tot}} = \Delta_c a^\dagger a + \omega_m b^\dagger b - g_0 a^\dagger a(b^\dagger + b) - g_{\mathrm{ck}} a^\dagger a b^\dagger b + i\Omega(a^\dagger - a), \tag{3}$$

where the detuning is $\Delta_c = \omega_c - \omega_l$.

The statistical properties of photons can be characterized by calculating the second-order correlation function of photons

$$g^{(2)}(t,\tau) = \frac{\langle a^\dagger(t) a^\dagger(t+\tau) a(t+\tau) a(t)\rangle}{\langle a^\dagger(t) a(t)\rangle\langle a^\dagger(t+\tau) a(t+\tau)\rangle}. \tag{4}$$

In the steady state, the equal-time second-order correlation function is given by $g^{(2)}(0) = \mathrm{Lim}_{t\to\infty} g^{(2)}(t,0)$ and the delayed-time second-order correlation function is $g^{(2)}(\tau) = \mathrm{Lim}_{t\to\infty} g^{(2)}(t,\tau)$. The values of $g^{(2)}(0)$ can be used to investigate the quantum behavior of photons. When $g^{(2)}(0) > 1$, it indicates that the photon bunching effect with the super-Poissonian statistics occurs. On the contrary, when $g^{(2)}(0) < 1$, the photons tend to exhibit an antibunching effect with the sub-Poissonian statistics.

3. The Nonlinear Coupling-Induced Photon Blockade

3.1. Approximate Analytical Results

In this section, we first develop an approximately analytical expression for the second-order correlation function of the photons and then compare it with the numerical result. In the weak driving condition, that is, the driving strength ε_l is far smaller than the optical dissipation rate κ, the average number of photons inside the cavity are relatively small. Therefore, it is reasonable to only consider the few-photon subspace, e.g., $|0\rangle_a$, $|1\rangle_a$, $|2\rangle_a$. And the corresponding number states of the mechanical mirror do not need to be limited in quantity in theoretical calculations. In this case, we can expand the wave function of the system with the ansatz

$$|\varphi\rangle = \sum_{m=0}^{\infty} C_{0,m}|0\rangle_a|\tilde{m}(0)\rangle_b + \sum_{m=0}^{\infty} C_{1,m}|1\rangle_a|\tilde{m}(1)\rangle_b + \sum_{m=0}^{\infty} C_{2,m}\,|2\rangle_a|\tilde{m}(2)\rangle_b, \tag{5}$$

where the coefficients $C_{n,m}(n = 0,1,2)$ denote the probability amplitudes corresponding to the states $|n\rangle_a|\tilde{m}(n)\rangle_b(n = 0,1,2)$. The system dissipations can be treated by the effective non-Hermitian Hamiltonian

$$H_{\mathrm{eff}} = H_{\mathrm{tot}} - i\frac{\kappa}{2} a^\dagger a. \tag{6}$$

By substituting the state $|\varphi\rangle$ and the effective Hamiltonian H_{eff} into the Schrödinger equation $i|\dot{\varphi}\rangle = H_{\text{eff}}|\varphi\rangle$, we get the dynamic equations of motion for the coefficients in Equation (5):

$$\begin{aligned}
\dot{C}_{0,m} &= -i\tilde{E}_{0,m}C_{0,m} - \Omega\sum_{m=0}^{\infty}\langle l|\tilde{m}(1)\rangle_b C_{1,m}, \\
\dot{C}_{1,m} &= -(i\tilde{E}_{1,m} + \frac{\kappa}{2})C_{1,m} + \Omega\sum_{l=0}^{\infty}\langle\tilde{m}(1)|l\rangle_b C_{0,m} - \sqrt{2}\Omega\sum_{l=0}^{\infty}\langle\tilde{m}(1)|\tilde{l}(2)\rangle_b C_{2,l}, \\
\dot{C}_{2,m} &= -(i\tilde{E}_{2,m} + \kappa)C_{2,m} + \sqrt{2}\Omega\sum_{l=0}^{\infty}\langle\tilde{m}(2)|\tilde{l}(1)\rangle_b C_{1,l}.
\end{aligned} \tag{7}$$

For the state given by Equation (5), the steady-state equal-time second-order correlation function can be written as

$$g^{(2)}(0) = \frac{2\sum_{m=0}^{\infty}|C_{2,m}|^2}{(\sum_{m=0}^{\infty}|C_{1,m}|^2 + 2\sum_{m=0}^{\infty}|C_{2,m}|^2)^2} \approx \frac{2\sum_{m=0}^{\infty}|C_{2,m}|^2}{(\sum_{m=0}^{\infty}|C_{1,m}|^2)^2}. \tag{8}$$

The second relation in Equation (8) follows from the weak-driving approximation. $\Omega \ll 1$, the one- and two-photon probability amplitudes scale as $C_{1,m} \propto \Omega$ and $C_{2,m} \propto \Omega^2$, respectively. Consequently, $\sum_m |C_{1,m}|^2 \propto \Omega^2$, $\sum_m |C_{2,m}|^2 \propto \Omega^4$. Therefore, the two-photon contribution in the denominator of Equation (8) is of higher perturbative order and can be neglected to the lowest nonvanishing order. After this approximation, the explicit factor Ω^4 cancels between the numerator and denominator. In the regime. Under weak driving conditions, a perturbation method can be used to solve the probability amplitudes of Equation (5) and the steady-state solutions can be achieved (see Appendix A for derivation details). Ultimately, we obtain the analytical result of the steady-state equal-time second-order correlation function

$$g^{(2)}(0) = \frac{4(\Delta_c - \delta^{(1)})^2 + \kappa^2}{(2\Delta_c - \delta^{(2)})^2 + \kappa^2}. \tag{9}$$

Equation (9) is therefore the leading-order result in the weak-driving regime. For stronger driving, the full denominator, higher-order corrections to the probability amplitudes, and higher-photon-number excitations generally introduce an explicit dependence of $g^{(2)}(0)$ on Ω. According to this analytical expression of the second-order correlation function, different quantum effects can be observed by adjusting the driving detuning. For example, when the optical driving field satisfies the single-photon resonant condition, i.e., $\Delta_c = \delta^{(1)}$, one can yield

$$g^{(2)}(0) = \frac{\kappa^2}{(2\delta^{(1)} - \delta^{(2)})^2 + \kappa^2}. \tag{10}$$

It is obvious that because of $\delta^{(2)} > 2\delta^{(1)}$, i.e., $\delta^{(2)} - 2\delta^{(1)} \neq 0$, one can yield $g^{(2)}(0) < 1$, which implies a photon antibunching effect. Furthermore, for $\delta^{(2)} - 2\delta^{(1)} \gg \kappa$, the values of $g^{(2)}(0)$ can be much smaller than 1 and a strong photon blockade occurs. In contrast, it can be seen from Equation (9) that in the case of two-photon resonant driving, i.e., $\Delta_c = \delta^{(2)}/2$, one can have $g^{(2)}(0) = [(\delta^{(2)} - 2\delta^{(1)})^2 + \kappa^2]/\kappa^2$, which is always larger than 1 and corresponds to the situation of photon bunching effect.

3.2. Numerical Results

When considering environmental effects, the dissipative dynamics of the Laguerre–Gaussian (LG) optorotational system with cross-Kerr nonlinearity can be described by the master equation

$$\frac{\partial\rho}{\partial t} = -i[H_{\mathrm{tot}},\rho] + \kappa\mathcal{D}[a]\rho + \gamma_m(n_{\mathrm{th}}+1)\mathcal{D}[b]\rho + \gamma_m n_{\mathrm{th}}\mathcal{D}[b^\dagger]\rho, \tag{11}$$

where $\mathcal{D}[o]\rho = o\rho o^\dagger - \frac{1}{2}(o^\dagger o\rho + \rho o^\dagger o)$ is the standard Lindblad superoperator, γ_m is the decay rate of the mechanical rotating mirror, $n_{\mathrm{th}} = [\exp(\hbar\omega_m/k_B T) - 1]^{-1}$ is the average thermal phonon number and T is the temperature of the heat bath.

In Figure 3, we plot the steady-state equal-time second-order correlation function $g^{(2)}(0)$ versus the driving detuning Δ_c/κ. The red solid line corresponds to the numerical result based on the master equation. By numerically solving the master equation in Equation (11), the steady-state operator ρ_{ss} corresponding to the system and the expression of the second-order correlation function can be obtained, while the blue dashed curve describes the analytical solution of Equation (9). First, it can be seen from Figure 3 that the numerical result agrees well with the analytical result. In addition, the curves exhibit several peaks and dips. Among them, the deepest dip describes the case of single photon resonant driving, i.e., the detuning is $\Delta_c = \delta^{(1)}$, where $g^{(2)}(0) \ll 1$. This accurately manifests the photon blockade effect. Qualitatively, this phenomenon can be understood from the energy-level diagram in Figure 2. When the driving field is on resonance with the $|0\rangle_a|\tilde{0}(0)\rangle_b \to |1\rangle_a|\tilde{0}(1)\rangle_b$ transition, the same $|1\rangle_a|\tilde{0}(1)\rangle_b \to |2\rangle_a|\tilde{0}(2)\rangle_b$ transition is detuned and will be suppressed. Therefore, a significant photon blockade effect phenomenon occurs. Note that in Figure 3 there is a dip on the far left of the curve, where the value of $g^{(2)}(0)$ is smaller than 1, which indicates a photon antibunching effect. Actually, it describes the $|0\rangle_a|\tilde{0}(0)\rangle_b \to |1\rangle_a|\tilde{1}(1)\rangle_b$ transition process at $\Delta_c = \delta^{(1)} - (\omega_m - g_{\mathrm{ck}})$ with a photon and a phonon involved. Due to the energy anharmonicity, the two-photon transition is hindered. In contrast, there are three peaks with $g^{(2)}(0)_{\mathrm{ss}} \gg 1$, as shown in Figure 3. The detunings at these peaks from right to left are $\Delta_c/\kappa = \delta^{(2)}/2$, $\Delta_c/\kappa = [\delta^{(2)} - (\omega_m - g_{\mathrm{ck}})]/2$ and $\Delta_c/\kappa = [\delta^{(2)} - 2(\omega_m - g_{\mathrm{ck}})]/2$, respectively. They demonstrate the case of the two-photon resonant driving. And the corresponding transition processes are $|0\rangle_a|\tilde{0}(0)\rangle_b \to |2\rangle_a|\tilde{0}(2)\rangle_b$, $|0\rangle_a|\tilde{0}(0)\rangle_b \to |2\rangle_a|\tilde{1}(2)\rangle_b$, and $|0\rangle_a|\tilde{0}(0)\rangle_b \to |2\rangle_a|\tilde{2}(2)\rangle_b$, which lead to the appearance of the photon bunching effect. Compared to the situation of phonons involved, when phonons are not involved, i.e., $\Delta_c/\kappa = \delta^{(2)}/2$, the value of $g^{(2)}(0)$ is larger. This indicates that the photon bunching effect is much stronger than that of phonons involved.

To study the influence of cross-Kerr nonlinearity on the photon statistical properties, Figure 4 shows the steady state second-order correlation function $g^{(2)}(0)$ as a function of the cavity detuning Δ_c/κ for different cross-Kerr strengths g_{ck}. In these figures of Figure 4, the blue dashed curve corresponds to the reference case of $g_{\mathrm{ck}} = 0$, while the red solid curve displays the results in the presence of cross-Kerr coupling. It can be found that the deepest antibunching dip and the prominent bunching peak are associated with the single-photon and two-photon resonance, respectively. In our numerical treatment, these resonances occur at the detuning $\Delta_c = \delta^{(1)}$, $\Delta_c = \delta^{(2)}/2$, corresponding to the optimal single-photon blockade and the opening of the two-photon excitation channel. Specifically, in the absence of cross-Kerr nonlinearity, i.e., $g_{\mathrm{ck}} = 0$, the single-photon blockade and the two-photon resonant driving is $\Delta_c = g_0^2/\omega_m$ and the two-photon resonant driving is $\Delta_c = 2g_0^2/\omega_m$. When cross-Kerr interaction is introduced, the mechanical frequency seen by the n photon manifold is renormalized to $\omega_m - ng_{\mathrm{ck}}$. As a result, the single-photon and two-photon resonant conditions are shifted to $\Delta_c = g_0^2/(\omega_m - g_{\mathrm{ck}})$, $\Delta_c = 2g_0^2/(\omega_m - 2g_{\mathrm{ck}})$, respectively, which show that both resonances are pushed towards larger Δ_c, and the two-photon resonance moves away from the single-photon resonance more rapidly as cross-Kerr strength g_{ck} increases. These results are also verified in Figure 4a–d. In Figure 4a, when the cross-Kerr coupling is relatively weak, e.g., $g_{\mathrm{ck}} = 0.5\kappa$, the red curve exhibits a slightly deeper antibunching dip at the single-photon resonant driving $\Delta_c = \delta^{(1)}$ compared with the case of $g_{\rm ck} = 0$. This indicates that a small cross-Kerr interaction can enhance photon blockade at the optimal single-photon resonant condition. Indeed, it originates from the fact that the cross-Kerr nonlinearity term can enhance the effective optical nonlinearity and further suppress two-photon excitation pathways. When the cross-Kerr interaction is increased to $g_{\rm ck} = \kappa$, as shown in Figure 4b, the value of the second-order correlation function $g^{(2)}(0)$ is still smaller than that for $g_{\rm ck} = 0$. However, in Figure 4c,d, a further increase in $g_{\rm ck}$ no longer improves the blockade effect at $\Delta_c = \delta^{(1)}$. Instead, the value of $g^{(2)}(0)$ at the single-photon resonance starts to increase and can even become larger than that in the case of $g_{\rm ck} = 0$. These phenomena illustrate that $g_{\rm ck}$ is not a "the larger, the better" parameter for generating the photon quantum effect. In other words, the cross-Kerr interaction has a non-monotonic impact on the photon statistics. Therefore, there exists a limited window with moderate cross-Kerr strengths where the photon blockade effect at $\Delta_c = \delta^{(1)}$ can be optimally enhanced.

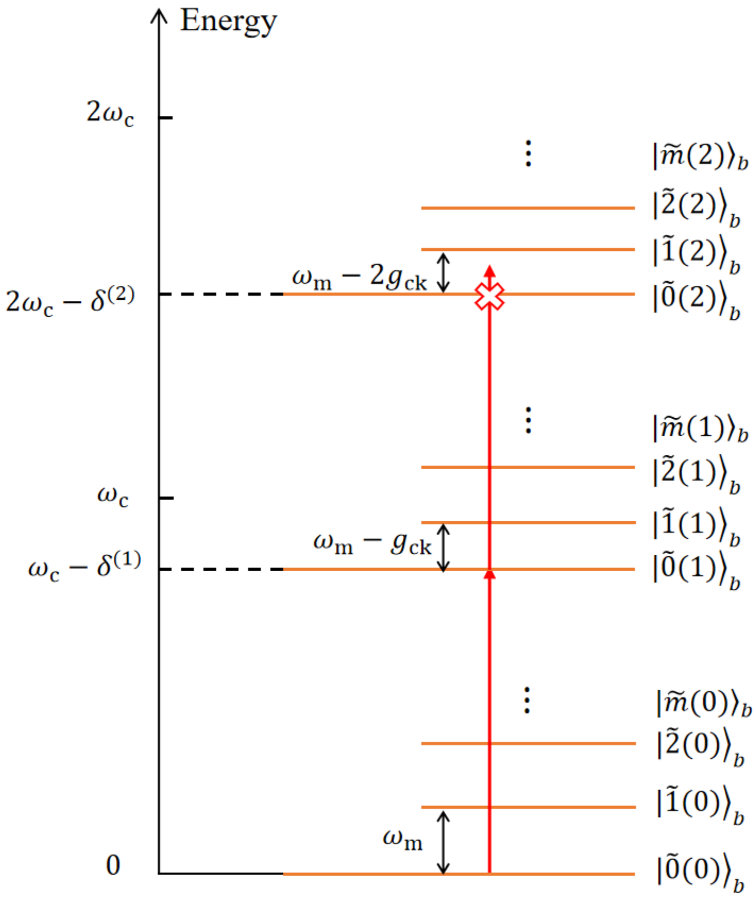

Figure 2. Schematic diagram of energy level structure of the Laguerre–Gaussian optorotational cavity with cross-Kerr nonlinearity. The vertical axis represents the energy. The system eigenvalues are $E_{n,m} = n\omega_c + (\omega_m - ng_{\rm ck})m - \delta^{(n)}$, where n, m are photon numbers and phonon numbers, respectively, and $\delta^{(n)} = g_0^2 n^2/(\omega_m - ng_{\rm ck})$. The corresponding eigenstates are $|n\rangle_a|\tilde{m}(n)\rangle_b$, where $|n\rangle_a$ are photon number states of the cavity mode a. Each cluster of orange energy levels correspondences to a fixed number of photons $n = 0, 1, 2, \ldots$. For the case of n photons, the mechanical states are the n-photon displaced number states $|\tilde{m}(n)\rangle_b$ for mode b, where the effective frequency of the mechanical mode in the n photon manifold is renormalized to $\omega_m - ng_{ck}$. The red solid arrow denotes the optical transition driving. Due to the energy-level anharmonicity, when the driving field is on resonance with the $|0\rangle_a|\tilde{0}(0)\rangle_b \to |1\rangle_a|\tilde{0}(1)\rangle_b$ transition, the same $|1\rangle_a|\tilde{0}(1)\rangle_b \to |2\rangle_a|\tilde{0}(2)\rangle_b$ transition is detuned.

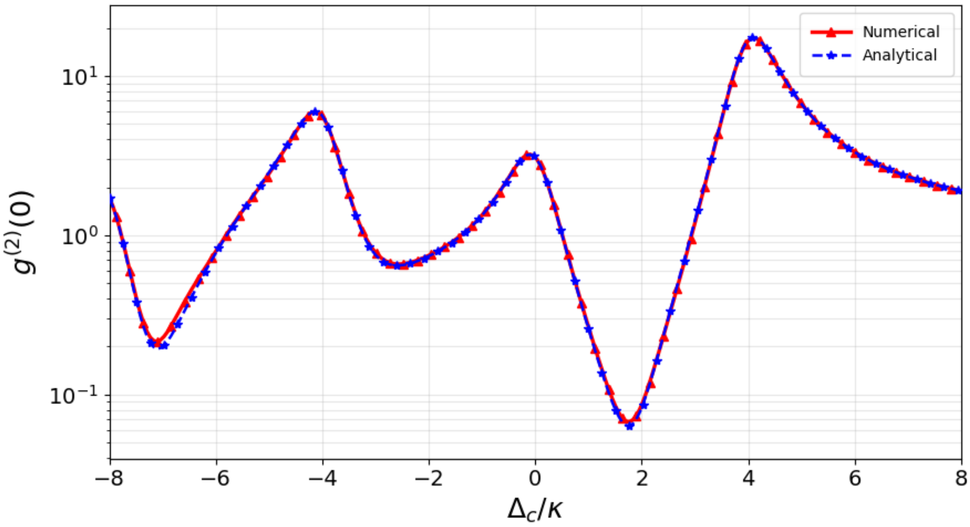

Figure 3. The steady-state equal-time second order correlation function $g^{(2)}(0)$ versus the detuning Δ_c/κ. The blue dotted curve represents the analytical solution of $g^{(2)}(0)$, and the red solid curve corresponds to the numerical solution of $g^{(2)}(0)$. The system parameters we take are $g_0/\kappa = 4.0$, $g_{\rm ck}/\kappa = 1.0$, $\omega_m/\kappa = 10.0$, $\Omega/\kappa = 0.01$, and $\gamma_m/\kappa = 0.001$, $n_{th} = 0$.

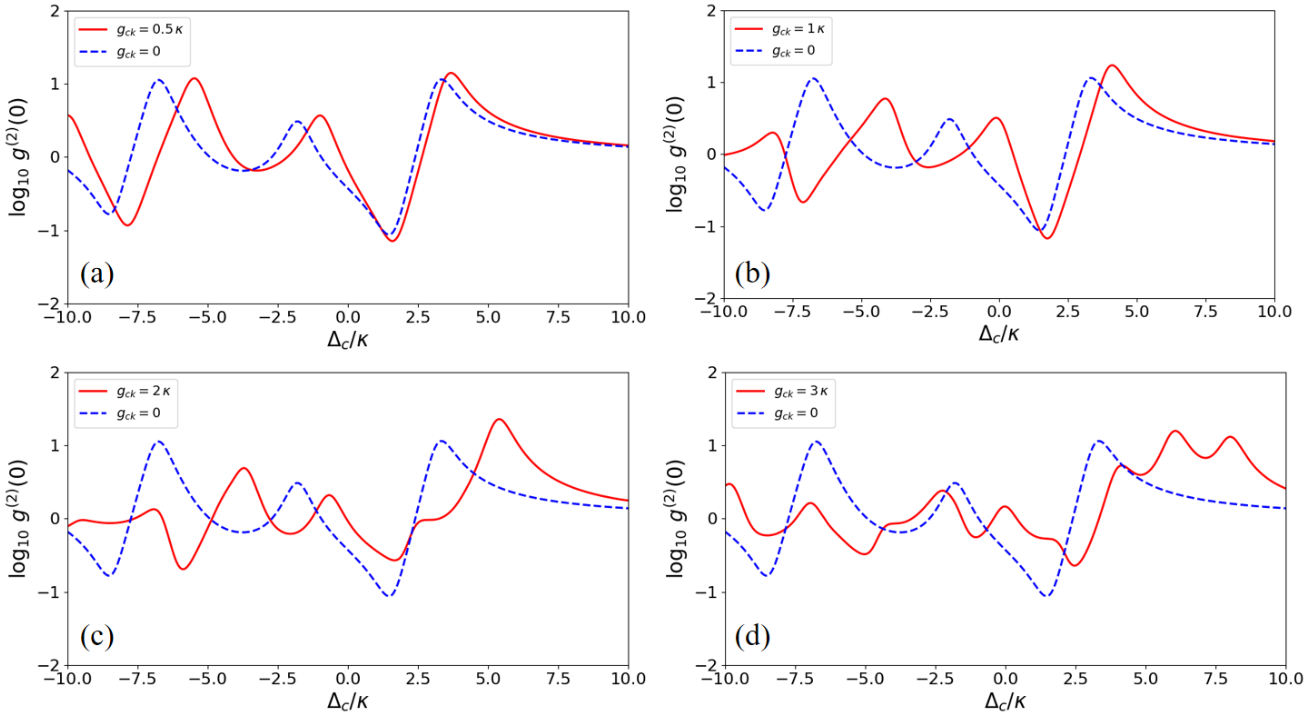

Figure 4. The second-order correlation function versus the detuning Δ_c/κ for different cross-Kerr coupling strength g_{ck}. The values of the cross-Kerr coupling strength from (**a**–**d**) are $g_{ck} = 0.5\kappa, 1\kappa, 2\kappa, 3\kappa$, respectively. The system parameters are $g_0/\kappa = 4.0$, $\omega_m/\kappa = 10.0$, $\Omega/\kappa = 0.01$, and $\gamma_m/\kappa = 0.001$, $n_{th} = 0$.

In order to further explore how nonlinear interactions affect the statistical properties of photons, we plot the steady state second-order correlation function $g^{(2)}(0)$ as a function of the optomechanical coupling strength g_0/κ and the cross-Kerr coupling strength $g_{\rm ck}/\kappa$ under the single-photon resonant condition in Figure 5a. It clearly shows that when the values of g_0 are small, e.g., $g_0/\kappa < 0.5$, photons almost exhibit Poissonian statistical characteristics with $g^{(2)}(0) \approx 1$ regardless of how strong the cross-Kerr strengths $g_{\rm ck}/\kappa$ are. With the increase in g_0, the system gradually presents sub-Poissonian statistics for the photons, as indicated by the light-blue regions. In these regions, strong photon antibunching effect with $g^{(2)}(0) \ll 1$ and even photon blockade effect with $g^{(2)}(0) \to 0$ can be observed. Meanwhile, it can be evidently found that some red regions with $g^{(2)}(0) \gg 1$ appear even though the coupling parameters g_0/κ and $g_{\rm ck}/\kappa$ are in the strong coupling regime. Actually, it is the result of phonon-assisted multiphoton resonances, where additional two-photon or multi-photon excitation channels are opened and the photons tend to bunch together. From the eigenenergy spectrum $E_{n,m} = n\omega_c + (\omega_m - ng_{\rm ck})m - \delta^{(n)}$, it can be seen that the effective mechanical frequency in the n-photon manifold is $\omega_m^{(n)} = \omega_m - ng_{\rm ck}$. The parameters are required to satisfy the condition of $\omega_m - 2g_{\rm ck} > 0$ to guarantee the relevant stability. Since the photon-transition process in the weak-driving regime is mainly governed by the zero-, one-, and two-photon manifolds, the parameter condition is $\omega_m - 2g_{\rm ck} > 0$, or equivalently $g_{\rm ck} < \omega_m/2$. For the parameters used in our numerical calculations, e.g., $\omega_m/\kappa = 10$, this condition gives $g_{\rm ck}/\kappa < 5$.

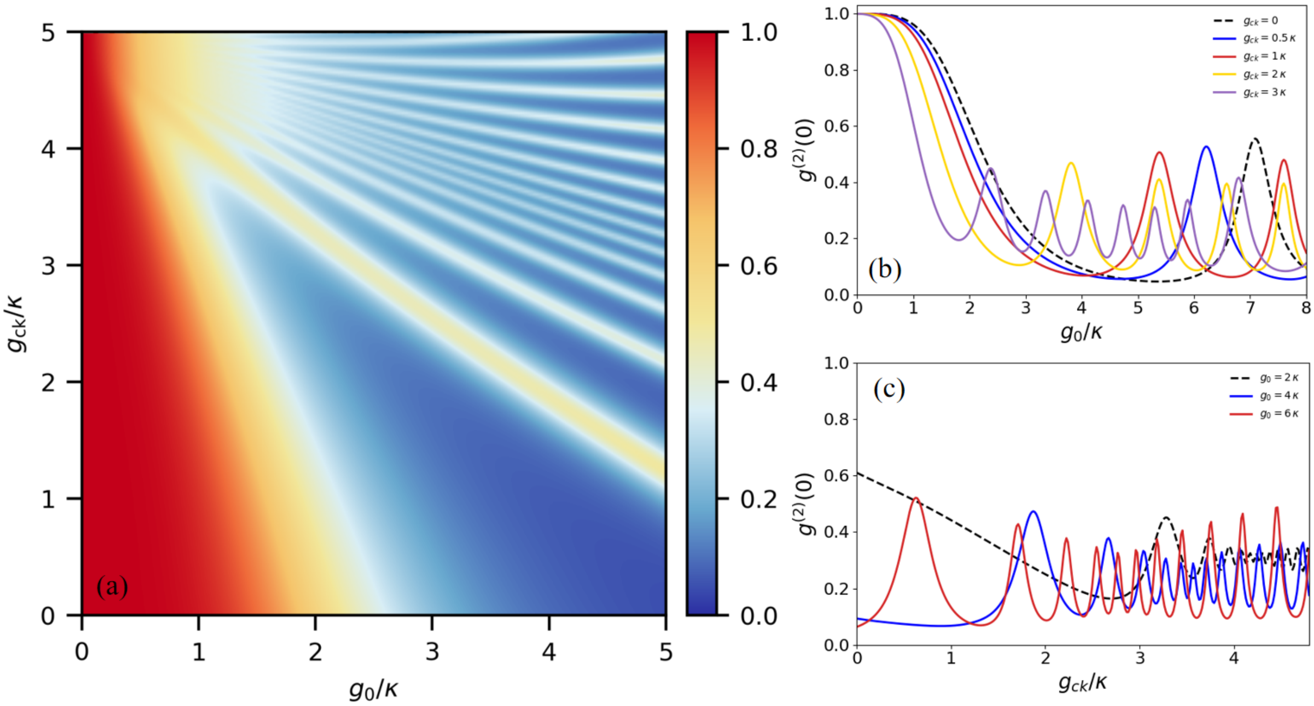

Figure 5. (**a**) Variation of second order correlation function $g^{(2)}(0)$ with the optorotational coupling g_0/κ and the cross-Kerr coupling $g_{\rm ck}/\kappa$. (**b**) Variation of the second-order correlation function $g^{(2)}(0)$ with the coupling strength g_0/κ for different cross-Kerr strengths $g_{\rm ck}/\kappa$. (**c**) Variation of the second-order correlation function $g^{(2)}(0)$ with the cross-Kerr strengths $g_{\rm ck}/\kappa$ for different coupling strength g_0/κ. The results in (**a**–**c**) are obtained in the case of single-photon resonant driving.

To more clearly observe the influence of nonlinear coupling, in Figure 5b we plot the steady state second-order correlation function $g^{(2)}(0)$ versus the optomechanical coupling strength g_0/κ for different cross-Kerr coupling strength $g_{\rm ck}/\kappa$ at the single-photon resonant point. The black dotted line, the blue solid line, the red solid line, the yellow solid line and the purple solid line correspond to the case of $g_{\rm ck}/\kappa = 0, 0.5, 1, 2, 3$, respectively. Firstly, it can be observed that when the values of g_0 start increasing from 0, these curves initially decrease gradually and the value of $g^{(2)}(0)$ can be much smaller than 1. Moreover, compared to the case of $g_{\rm ck} = 0$, the slopes of the other four curves in the presence of $g_{\rm ck}$ are steeper. This indicates that the presence of cross-Kerr coupling can enhance the generation of photon quantum effects. In addition, as the values of g_0 continue to increase, these curves exhibit a series of oscillations with several resonant peaks. Physically, this is because the mechanical phonons participate in the resonant excitation of the two-photon state, which increases the probability of the occurrence of the two-photon state. Therefore, the values of the second-order correlation function form a series of peaks. Next, we will quantitatively analyze the positions of these resonant peaks involving phonon sidebands. In the case of single-photon resonant transition ($|0\rangle_a|\tilde{0}(0)\rangle_b \rightarrow |1\rangle_a|\tilde{0}(1)\rangle_b$), the driving frequency satisfies $\Delta_c = \delta^{(1)}$. At this point, the m-phonon-assisted two-photon resonance transition ($|0\rangle_a|\tilde{0}(0)\rangle_b \rightarrow |2\rangle_a|\tilde{m}(2)\rangle_b$) can occur simultaneously. According to the calculation, it can be derived that the functional relationship among the optomechanical coupling strength g_0, the cross-Kerr coupling strength g_{ck} and the number of mechanical phonons m is

$$g_0(m) = \sqrt{\frac{m}{2\omega_m}(\omega_m - g_{ck})(\omega_m - 2g_{ck})^2}, \tag{12}$$

where $m = 1, 2, 3, \ldots$. That is, when the values of parameters satisfy this equation, two-photon resonant transition induced by phonon sidebands occurs. In the regions between adjacent peaks in Figure 5b, these resonance conditions are no longer satisfied for a mechanical phonon number m, and the phonon-assisted enhancement of the two-photon excitation is therefore suppressed. As a result, photon blockade effect is partially restored, giving rise to the dip structures. In particular, in the absence of cross-Kerr coupling, Equation (12) is simplified to $g_0 = \sqrt{m/2\omega_m}(m = 1, 2, 3, \ldots)$, which is the result of phonon-induced tunneling in a typical optomechanical system. This can be seen from Equation (12) that with the increase for specific phonon number m. Therefore, the positions of these resonant peaks displayed in Figure 5b exhibit a trend of shifting to the left. This phenomenon can be evidently observed from the first resonant peak ($m = 1$). Moreover, when the values of g_{ck} increase, the number of resonance peaks in the curves of Figure 5b also increases and the spacing between neighboring peaks becomes smaller, which can be easily explained from Equation (12).

In Figure 5c, we show the dependence of the second-order correlation function $g^{(2)}(0)$ on the cross-Kerr coupling g_{ck}/κ in the case of the single-photon resonance for three fixed values of the optomechanical coupling g_0. When $g_0 = 4\kappa$, as depicted by the blue solid line, the values of $g^{(2)}(0)$ at $g_{\mathrm{ck}} = 0.5\kappa$, κ are smaller that when $g_{\mathrm{ck}} = 0$. However, when $g_{\mathrm{ck}} = 2\kappa$, 3κ, the values of $g^{(2)}(0)$ are bigger than that in the absence of cross-Kerr nonlinearity. These results are consistent with that in Figure 4. It is obvious that the photon statistical properties have a non-monotonic dependence on the optomechanical coupling. From the perspective of analytical results, when $\Delta_c = \delta^{(1)}$, the expression of the second-order correlation function is as shown in Equation (10). By defining $U_{\mathrm{eff}} = \delta^{(1)} - \delta^{(2)}/2$, Equation (10) can be written as

$$g^{(2)}(0) = \frac{\kappa^2}{(2U_{\mathrm{eff}})^2 + \kappa^2}, \tag{13}$$

where

$$U_{\mathrm{eff}} = -\frac{g_0^2\omega_m}{(\omega_m - g_{\mathrm{ck}})(\omega_m - 2g_{\mathrm{ck}})}. \tag{14}$$

This quantity characterizes the anharmonic detuning between the single-photon resonance and the two-photon resonance driving. It can be seen that away from the phonon-assisted resonance point, increasing g_{ck} will enlarge the detuning $|U_{\mathrm{eff}}|$, which suppresses $g^{(2)}(0)$ and strengthens photon antibunching. This explains the initial decreasing tendency of the curves. However, the increase in g_{ck} simultaneously reduces the effective phonon sideband spacing $\omega_m - 2g_{\mathrm{ck}}$, which increases the probability of the transition to the two-photon state $|2\rangle_a|\tilde{m}(2)\rangle_b$. The phonon-assisted resonance condition $2U_{\mathrm{eff}} = -m(\omega_m - 2g_{\mathrm{ck}})$ can be satisfied for successive sideband orders $m(m = 1, 2, 3, \ldots)$. As a result, each resonant peak in the curves of $g^{(2)}(0)$ can be actually associated with a specific phonon sideband m. To make this correspondence more explicit, the positions of these peaks extracted from Figure 5c for $g_0 = 2\kappa$ and $g_0 = 4\kappa$ are summarized in Tables 1 and 2, respectively. Specifically, when $g_0 = 2\kappa$, the black dashed curve exhibits a pronounced decreasing trend over a wide range of parameters (e.g., $g_{\rm ck} \leq 2.6\kappa$). Consequently, the photon blockade effect is gradually strengthened with the increase in $g_{\rm ck}$. And the first phonon-assisted resonant peak appears at a relatively large cross-Kerr coupling, around $g_{\rm ck} \approx 3.28\kappa$, as shown in Table 1. For $g_0 = 4\kappa$, the same suppression mechanism is still present at a relatively low $g_{\rm ck}$, but the cross-Kerr coupling strength corresponding to the first resonance peak shifts to a smaller value, $g_{\rm ck} \approx 1.87\kappa$. So the initially monotonic decrease in the curve is interrupted earlier by two-photon-resonance-induced peaks. For $g_0 = 6\kappa$, the first resonance peak occurs at $g_{\rm ck} \approx 0.62\kappa$, indicating that the improvement range of the photon antibunching induced by a weak cross-Kerr nonlinearity $g_{\rm ck}$ becomes very narrow and that the curve is quickly dominated by phonon-assisted resonances. These results fully demonstrate that the competition between the optomechanical coupling strength and the cross-Kerr coupling strength dominates the photon quantum behaviors. In other words, the achievement of the photon blockade effect requires the cooperative control between the optomechanical coupling and the cross-Kerr coupling instead of any individual part.

Table 1. The positions of peaks in Figure 5c and the corresponding values of $g^{(2)}(0)$ in the case of $g_0 = 2\kappa$.

m	1	2	3	4	5	6	7
g_{ck}/κ	3.284	3.740	3.952	4.082	4.173	4.242	4.307
$g^{(2)}(0)$	0.483	0.408	0.378	0.363	0.354	0.350	0.355

Table 2. The positions of peaks in Figure 5c and the corresponding values of $g^{(2)}(0)$ in the case of $g_0 = 4\kappa$.

m	1	2	3	4	5	6	7
g_{ck}/κ	1.873	2.669	3.045	3.277	3.440	3.571	3.708
$g^{(2)}(0)$	0.541	0.443	0.394	0.361	0.343	0.346	0.371

Based on the above discussion, the single photon optorotational coupling strength $g_0 = g_\phi\sqrt{\hbar/2I\omega_m}$ is a crucial parameter to observe the photon quantum behavior. Here $g_\phi = cl/L$ is the optorotational coupling parameter, where c is the speed of light in vacuum, l is the topological charge value and L is the LG cavity length. Combing with $I = \frac{1}{2}MR^2$, the single photon optorotational coupling strength can be expressed as

$$g_0 = \frac{cl}{L}\sqrt{\frac{\hbar}{MR^2\omega_m}}. \tag{15}$$

It can be seen that g_0 is proportional to the topological charge l. Therefore, by changing the topological charge in the injection cavity, the optomechanical coupling strength can be controllably adjusted without changing the cavity length and other mechanical parameters. Compared with the traditional way of adjusting g_0 by changing the length or quality of the cavity mirror, using the topological charge as the controllable parameter is more flexible in experiments. In Figure 6, the second-order correlation function $g^{(2)}(0)$ is plotted as a function of the topological charge l for $g_{\rm ck} = 0$ and $g_{\rm ck} = \kappa$, as shown by the black dashed curve and the blue solid curve, respectively. It shows that the increase in the topological charge l will eventually lead to the strong photon antibunching $g^{(2)}(0) \ll 1$ and even the photon blockade $g^{(2)}(0) \to 0$, as shown by the initial decline of the curve. And by comparing the two cases of $g_{\rm ck} = 0$ and $g_{\rm ck} = \kappa$, it is found that the introduction of $g_{\rm ck}$ will accelerate the reduction rate of the second-order correlation function to some extent. When the topological charge l further increases to a certain value, the system driving satisfies the conditions of phonon-assisted two-photon resonance. Thus, as expected, a series of peaks appear corresponding to the cases of $m = 1, 2, 3, \ldots$. In addition, the single photon optorotational coupling is also relevant to the mass M and the radius R of the rotating mirror. Specifically, it is $g_0 \propto \frac{1}{R\sqrt{M}}$, as seen from Equation (15), which indicates that the increase in radius R and mass M of the cavity mirror will result in the decrease in the coupling strength. The second order correlation function $\log_{10} g^{(2)}(0)$ versus the mass M and the radius R of the rear mirror is shown in Figure 7. It can be clearly observed that in the case of a relatively large R and M, the values of the second-order correlation function in this region are approximately 1, as depicted by the upper right corner of Figure 7. This is because the corresponding coupling strength is very weak, which hinders the generation of photon quantum behaviors. When either the mass M or the radius R is relatively small, the coupling strength will be enlarged, which corresponds to the left and bottom areas close to the coordinate axes in the image. In this case, a strong photon blockade phenomenon with $g^{(2)}(0) \to 0$ is yielded, as shown in the dark blue area. With the further decrease in system parameters M and R, the condition of the single photon resonance is close to that of phonon-assisted two-photon resonance. Therefore, the dark blue band representing the photon blockade and the light blue band representing two-photon resonance alternately appear within a certain range.

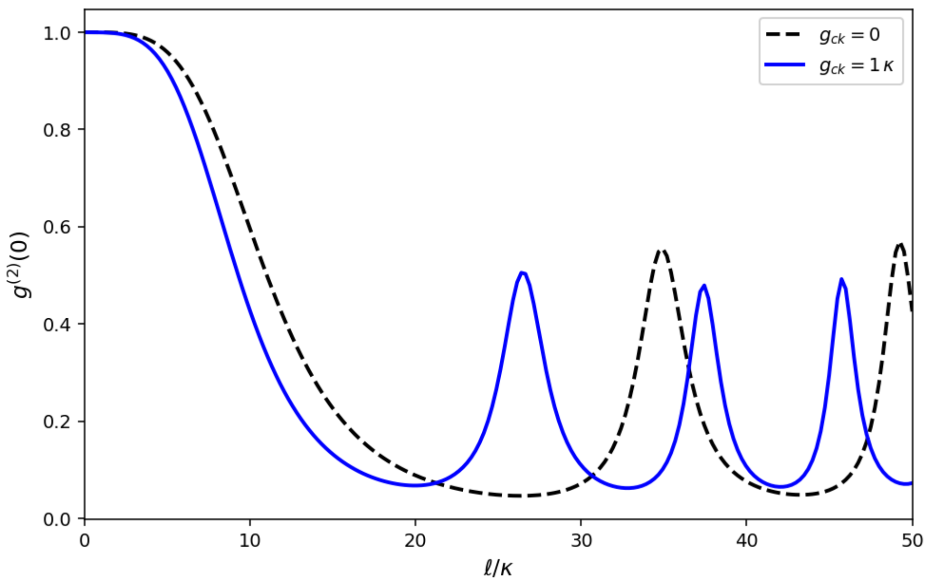

Figure 6. Influence of the topological charge l on the second order correlation function $g^{(2)}(0)$ in the case of single-photon resonant driving. The system parameters are the same as that in Figure 3.

In Figure 8a we show the dependence of the equal-time second-order correlation function $g^{(2)}(0)$ on the average thermal phonon number $n_{\rm th}$ under the single-photon resonance condition $\Delta_c = \delta^{(1)}$ for different cross-Kerr strengths. It is evident that the values of $g^{(2)}(0)$ increase monotonically with the thermal phonon number $n_{\rm th}$ in all cases, indicating that thermal fluctuations introduced by the mechanical bath progressively degrade the antibunching characteristics of the cavity field and hence weaken the photon blockade effect. A further comparison shows that a larger cross-Kerr nonlinearity leads to a more rapid increase in the curve of $g^{(2)}(0)$. This tendency is particularly pronounced for $g_{\rm ck} = 2\kappa$, implying that the system becomes more sensitive to thermal phonon fluctuations in the strong cross-Kerr regime. The underlying physical mechanism is that, under a fixed single-photon resonance driving condition, increasing the cross-Kerr strength reshapes the effective anharmonic spectrum and gradually brings the single-photon resonance closer to a phonon-assisted two-photon resonance channel. As the thermal phonon number increases, phonon-number fluctuations in the mechanical bath become stronger, making phonon-assisted two-photon transitions easier to activate. Consequently, the two-photon population is enhanced, which leads to a larger $g^{(2)}(0)$. In this sense, a sufficiently strong cross-Kerr interaction does not further improve photon blockade. On the contrary, by pushing the system closer to a phonon-assisted two-photon resonance, it amplifies the detrimental role of thermal noise in promoting multiphoton excitation and therefore weakens the single-photon blockade effect. Thus, to better observe the desired photon blockade, it requires cooling the rotating mechanical mirror to low temperature. In addition, one can see that even though the thermal phonon number n_{th} increases to a relatively large value, e.g., $n_{\mathrm{th}} = 10$, a strong photon antibunching phenomenon still exists. This indicates that the photon antibunching effect is robust against the thermal phonon number. To further clarify the influence of mechanical dissipation, Figure 8b presents $g^{(2)}(0)$ as a function of the mechanical damping rate γ_m/κ in the case of $n_{\mathrm{th}} = 5$. When the values of γ_m/κ change from 10^{-4} to 10^{-2}, the two curves of $g^{(2)}(0)$ corresponding to $g_{\mathrm{ck}} = 0$ and $g_{\mathrm{ck}} = \kappa$ have no significant change with $g^{(2)}(0) < 1$. In contrast, when $g_{\mathrm{ck}} = 2\kappa$, the curve of $g^{(2)}(0)$ has a relatively obvious trend of change with $g^{(2)}(0) > 1$, indicating that the photon blockade is broken under the combined effect of sideband renormalization induced by strong cross-Kerr interaction and mechanical dissipation. On the one hand, these results suggest that the mechanical dissipation will weaken the single-photon blockade effect. On the other hand, it reveals that the quantum statistical properties of photons is robust against the mechanical decoherence.

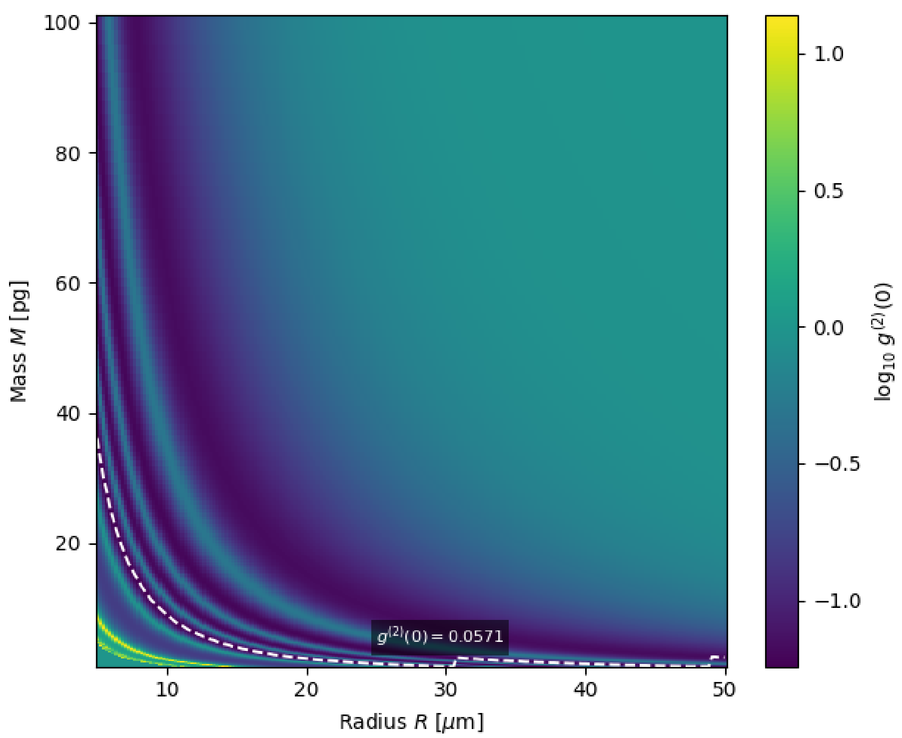

Figure 7. Variation of logarithm of second order correlation function $\log_{10} g^{(2)}(0)$ with mass M and radius R of the rotating mirror in the case of single-photon resonant driving. The white dotted line corresponds to the cases of $g^{(2)}(0) \approx 0.057$. The system parameters are the same as that in Figure 3.

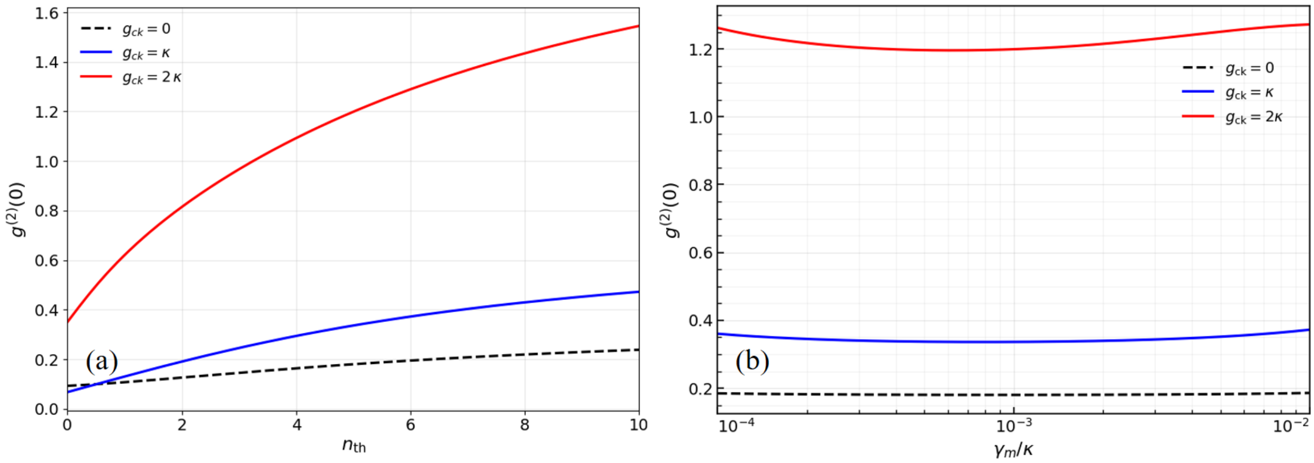

Figure 8. (**a**) The influence of the average thermal phonon number $n_{\rm th}$ and (**b**) the mechanical damping rate γ_m/κ on the second-order correlation function $g^{(2)}(0)$ under the single-photon resonance condition $\Delta_c = \delta^{(1)}$ for different cross-Kerr strengths. In (**b**), $n_{\rm th} = 5$. The other system parameters are the same as that in Figure 3.

Figure 9 presents the delayed-time second-order correlation function $g^{(2)}(\tau)$ as a function of the scaled time delay τ/κ^{-1}. First, the nonclassical character of photons in the LG cavity is clearly manifested by a small value of $g^{(2)}(0)$, i.e., $g^{(2)}(0) < 1$, corresponding to the sub-Poissonian statistics of photons. In addition, the curves with different values of $g_{\rm ck}$ show that $g^{(2)}(0) < g^{(2)}(\tau)$ as a signature of the photon antibunching effect. Furthermore, it can be observed that the curves of $g^{(2)}(\tau)$ exhibit a persistent oscillation. And with the increase in $g_{\rm ck}$, the fluctuation of curves is more obvious, as shown in the subgraph on the right side of Figure 9. Note that the values of $g^{(2)}(\tau)$ approach one in a long time delay τ, as expected. This indicates that the probability of two-photon excitations at the same time ($\tau = 0$) is smaller than that at a delay time ($\tau > 0$).

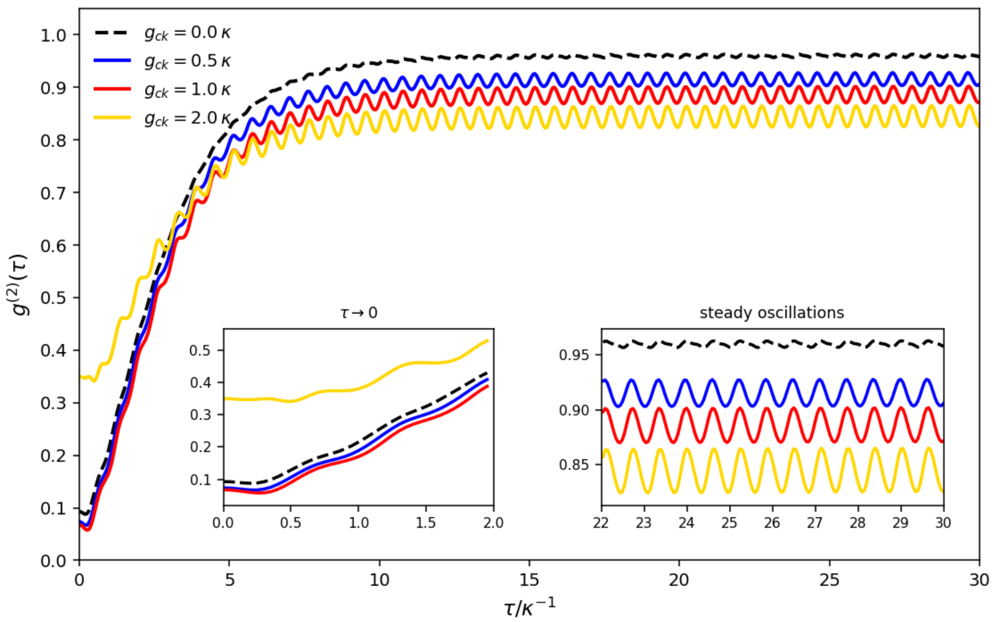

Figure 9. The delayed-time second-order correlation function $g^{(2)}(\tau)$ as a function of the scaled time delay τ/κ^{-1} under the single-photon resonance condition $\Delta_c = \delta^{(1)}$. The system parameters are the same as that in Figure 3.

4. Discussion

To place the present results in a broader context, Birnbaum et al. experimentally demonstrated photon blockade in a strongly coupled single-atom cavity-QED system and reported a transmitted-field correlation of $g^{(2)}(0) = 0.13 \pm 0.11$ under weak coherent excitation [16]. Although this platform differs from the present optorotational system, the experiment demonstrated that resolvable single-quantum energy-level anharmonicity can produce measurable photon antibunching and that the blockade can be directly characterized through Hanbury Brown–Twiss correlation measurements. The Birnbaum experiment is already included among the experimental photon blockade references in the present manuscript. For conventional radiation-pressure optomechanics, Rabl theoretically predicted pronounced photon antibunching under weak driving when the system approaches the single-photon strong-coupling and resolved-sideband regimes [26]. In this regime, the photon-number-dependent mechanical displacement induces an effective optical anharmonicity that suppresses the two-photon excitation channel. The analysis further showed that cavity broadening and finite thermal phonon occupation weaken the blockade by reducing the spectral resolution and activating additional phonon-assisted transitions. This work therefore provides a direct theoretical reference for the optical-loss and thermal-noise conditions considered in the present LG system. Rabl's work is the standard radiation-pressure optomechanical photon blockade reference adopted in our manuscript. For an engineered photon–phonon nonlinearity, Heikkilä et al. derived a Josephson-mediated interaction of the form $H_{\rm ck} = g_{\rm ck} a^\dagger a b^\dagger b$ and estimated $g_{\rm ck} \approx 0.25 g_0$ for representative circuit parameters [55]. Although this estimate was obtained for a superconducting circuit rather than an optical LG cavity, it provides a useful reference for the relative cross-Kerr strength adopted here: the representative parameters $g_0/\kappa = 4$ and $g_{\rm ck}/\kappa = 1$ correspond to $g_{\rm ck}/g_0 = 0.25$. In the present LG optorotational system, the minimum equal-time correlation reaches $g^{(2)}(0) \approx 0.057$. Moreover, Figure 8 shows that thermal phonon fluctuations and mechanical damping progressively weaken the blockade, with the degradation becoming more pronounced in the stronger cross-Kerr regime. The present work thus extends the generalized optomechanical photon blockade model from linear-momentum transfer to orbital-angular-momentum transfer and introduces the optical topological charge as an additional control parameter.

5. Conclusions

In conclusion, we explore the achievement of photon blockade effect in a Laguerre–Gaussian optorotational cavity with the typical optorotational coupling and cross-Kerr nonlinear coupling between the cavity mode and the rotating spiral phase mirror. The optorotational coupling in the LG system is induced by the exchange of orbital angular momentum. We investigate the statistical properties of photons by calculating the second-order correlation function numerically and analytically. The results show that to obtain the optimal photon blockade effect, it requires a strong coupling regime. And the presence of cross-Kerr nonlinearity can enhance the antibunching effect of photons to some extent. However, when either the optorotational coupling strength g_0 or the cross-Kerr nonlinear coupling strength $g_{\rm ck}$ is too large, the antibunching effect of photons cannot be further enhanced. In other words, the optimal photon blockade effect is dominated by a competitive and cooperative operation between the optorotational coupling and the cross-Kerr coupling instead of any strong individual part. In particular, in the case of single-photon resonant driving, phonon-assisted two-photon resonant transitions can occur with a strong nonlinearity g_0 or $g_{\rm ck}$, which will reduce the probability of single-photon resonant transition. Beyond coupling parameters, we consider the role of the inherent system parameters of the LG cavity on the photon blockade effect, including the optical topological charge l and the mirror properties such as the radius R and mass M. We show that these structural parameters can effectively reshape the coupling strength and the nonlinear energy spectrum, resulting in tunable antibunching landscapes for $g^{(2)}(0)$, which exhibits a distinct suppression regime and resonance shifts. In addition, we examine the influence of the mechanical environmental temperature. Increasing temperature introduces more thermal phonons and additional decoherence, which generally increases the values of $g^{(2)}(0)$ and thus weakens the photon blockade effect. Therefore, to obtain the desired photon blockade, it needs to decrease the temperature of thermal reservoir. Our work offers an alternative approach to manipulate the photon quantum behaviors in Laguerre–Gaussian optorotational systems and may have promising applications in quantum information processing based on LG systems utilizing the optical orbital angular momentum.

Author Contributions: Conceptualization, K.-D.L., T.-S.Y. and A.C.; methodology, T.-S.Y. and A.C.; software, K.-D.L.; formal analysis, K.-D.L. and T.-S.Y.; writing—original draft preparation, K.-D.L.; writing—review and editing, T.-S.Y. and A.C. All authors have read and agreed to the published version of the manuscript.

Funding: This work was supported by the National Natural Science Foundation of China (NSFC) (Grant No. 12575031).

Institutional Review Board Statement: Not applicable.

Informed Consent Statement: Not applicable.

Data Availability Statement: The original contributions presented in this study are included in the article. Further inquiries can be directed to the corresponding author.

Conflicts of Interest: The authors declare no conflicts of interest.

Appendix A

Appendix A.1. Derivation of Eigenequation

To solve the eigensystem corresponding to the Hamiltonian H, a displacement operator $D(\lambda)$ is introduced, where $D(\lambda)$ can be expressed as

$$D(\lambda) = \exp[\frac{g_0 a^\dagger a}{\omega_m - g_{\rm ck} a^\dagger a}](b^\dagger - b). \tag{A1}$$

According to the definition of photon number operator $n = a^\dagger a$, we can interpret λ as the mechanical displacement induced by n-photon number:

$$\lambda^{(n)} = \frac{n g_0}{\omega_m - n g_{\rm ck}}. \tag{A2}$$

By using displacement operators, the Hamiltonian can be diagonalized as

$$H' = \omega_c a^\dagger a + (\omega_m - g_{\rm ck} a^\dagger a) b^\dagger b - \frac{g_0^2 a^\dagger a a^\dagger a}{\omega_m - g_{\rm ck} a^\dagger a}. \tag{A3}$$

Similarly, we can use photon quantum number operator to describe the nonlinear terms of the transformed Hamiltonian H' energy level shift:

$$\delta = \frac{g_0^2 a^\dagger a a^\dagger a}{\omega_m - g_{\rm ck} a^\dagger a}, \delta^{(n)} = \frac{g_0^2 n^2}{\omega_m - n g_{\rm ck}}. \tag{A4}$$

By the above transformation, the eigenenergy levels and eigenvalues corresponding to the Hamiltonian of the system can be obtained:

$$H' |n\rangle_a |m\rangle_b = E_{n,m} |n\rangle_a |m\rangle_b, \tag{A5}$$

https://doi.org/10.3390/photonics13080725

where $|n\rangle_a$ and $|m\rangle_b(n, m = 1, 2, ...)$ correspond to the number states of the cavity mode and mechanical mode, respectively. The eigenvalues of a system can be expressed as

$$E_{n,m} = n\omega_c + (\omega_m - ng_{\text{ck}})m - \delta^{(n)}. \tag{A6}$$

When combining the mechanical oscillator free term and the cross-Kerr term in the Hamiltonian, it can be observed that the frequency of the mechanical oscillator changes with the number of photons contained in the cavity. In the eigenequation, the eigenvalue corresponding to the displaced number state of the mechanical oscillator $\omega'_m = \omega_m - ng_{\text{ck}}$, but the number of photons introduced will change the frequency of the mechanical oscillator, which will change the energy level corresponding to the mechanical oscillator. Therefore, it can be concluded that the number of photons in the cavity will change the eigensystem of mechanical oscillators, and the corresponding eigenstates of mechanical oscillators in the system need to be redefined:

$$|\tilde{m}(n)\rangle_b = D(\lambda^{(n)})|m\rangle_b. \tag{A7}$$

This is induced by the optorotational coupling and cross-Kerr nonlinear coupling. Finally, the eigenequation of this optorotational system can be written as

$$H'|n\rangle_a|\tilde{m}(n)\rangle_b = E_{n,m}|n\rangle_a|\tilde{m}(n)\rangle_b. \tag{A8}$$

Appendix A.2. Derivation of Approximate Analytical Results

By substituting the state $|\varphi\rangle$ of Equation (5) and the effective non-Hermitian Hamiltonian of Equation (6) into the Schrödinger equation $i|\dot{\varphi}\rangle = H_{\text{eff}}|\varphi\rangle$, a set of differential equations related to the probability amplitude coefficients can be obtained:

$$\begin{aligned}
\dot{C}_{0,m} &= -i\tilde{E}_{0,m}C_{0,m} - \Omega\sum_{m=0}^{\infty}\langle l|\tilde{m}(1)\rangle_b C_{1,m}, \\
\dot{C}_{1,m} &= -(i\tilde{E}_{1,m} + \frac{\kappa}{2})C_{1,m} + \Omega\sum_{l=0}^{\infty}\langle\tilde{m}(1)|l\rangle_b C_{0,m} - \sqrt{2}\Omega\sum_{l=0}^{\infty}\langle\tilde{m}(1)|\tilde{l}(2)\rangle_b C_{2,l}, \\
\dot{C}_{2,m} &= -(i\tilde{E}_{2,m} + \kappa)C_{2,m} + \sqrt{2}\Omega\sum_{l=0}^{\infty}\langle\tilde{m}(2)|\tilde{l}(1)\rangle_b C_{1,l}.
\end{aligned} \tag{A9}$$

In this system, optical driving will cause the mechanical oscillator states to change under the influence of different photon numbers, that is, to change its corresponding eigenvalues and eigenstates. These changed states are described using displaced number states, and the inner product of these displacement number states can be calculated by the Franck-Condon factor:

$$\left\langle\widetilde{m}(n_1)|\widetilde{l}(n_2)\right\rangle_b = \left\langle m|\exp[(\lambda^{(n_2)} - \lambda^{(n_1)})(b^\dagger - b)]|l\right\rangle_b (n_1, n_2 = 0, 1, 2), \tag{A10}$$

$$\langle n|D_b(x)|l\rangle_b = \begin{cases} \sqrt{\frac{n!}{l!}}e^{-\frac{|x|^2}{2}}(-x^*)^{l-n}L_n^{l-n}(|x|^2), l \geq n, \\ \sqrt{\frac{l!}{n!}}e^{-\frac{|x|^2}{2}}(x)^{n-l}L_l^{n-l}(|x|^2), n > l, \end{cases} \tag{A11}$$

where $D_b(x) = \exp(x^*b^\dagger - x^*b)$ is a displaced operator and L_n^l are the associated Laguerre polynomials.

In the case of weak driving, the perturbation method can be used to solve the probability amplitude coefficients $C_{0,m}$ of Equation (A10), and the influence of high-order terms can be ignored for each equation. Therefore, by integrating the time t of Equation (A10) from 0 to ∞, we can obtain

$$C_{0,m}(t) = C_{0,m}(0)e^{-i\tilde{E}_{0,m}t}, \tag{A12}$$

For the probability amplitude coefficients $C_{1,m}$ of Equation (A10), in order to facilitate the calculation, it is chosen to ignore higher-order terms. Performing the following Fourier transform $\mathcal{F}[\dot{C}_{1,m}(t)](\omega) = -i\omega\tilde{C}_{1,m}(\omega)$ on the equation yields

$$\tilde{C}_{1.m}(\omega) = \int_{-\infty}^{+\infty} C_{1,m}(t)e^{i\omega t}dt, \mathcal{F}[e^{-i\tilde{E}_{0,m}t}] = 2\pi\delta(\omega - \tilde{E}_{0,m}), \tag{A13}$$

$$\tilde{C}_{1.m}(\omega) = \frac{\Omega\sum_{l=0}^{\infty}\langle\tilde{m}(1)|l\rangle_b C_{0,m}(0)2\pi\delta(\omega - \tilde{E}_{0,m})}{-i(\omega - \tilde{E}_{0,m}) + i(\tilde{E}_{1,m} - \tilde{E}_{0,m}) + \frac{\kappa}{2}}. \tag{A14}$$

Further solved through frequency conversion:

$$C_{1,m}(t) = \Omega\sum_{l=0}^{\infty}\frac{\langle\tilde{m}(1)|l\rangle_b C_{0,l}(0)e^{-i\tilde{E}_{0,l}t}}{\tilde{E}_{1,m} - \tilde{E}_{0,l} - i\frac{\kappa}{2}}. \tag{A15}$$

Similarly, the same transformation is applied to the probability amplitude coefficients $C_{2,m}$ of Equation (A10):

$$C_{2,m}(t) = -\sqrt{2}\Omega^2\sum_{p,l=0}^{\infty}\frac{\langle\tilde{m}(2)|\tilde{l}(1)\rangle_b\langle\tilde{l}(1)|p\rangle_b C_{0,p}(0)e^{-i\tilde{E}_{0,p}t}}{(\tilde{E}_{2,m} - \tilde{E}_{0,p} - i\kappa)(\tilde{E}_{1,m} - \tilde{E}_{0,l} - i\frac{\kappa}{2})}. \tag{A16}$$

Therefore, under weak-driving conditions, defining the total occupation probability of the n-photon manifold as $P_{n=0,1,2} = \sum_{m=0}^{\infty}|C_{n,m}|^2$, the equal-time second-order correlation function can be expressed as $g^{(2)}(0) = 2P_2/(P_1 + 2P_2)^2 \approx 2P_2/P_1^2$, where the approximation follows from $P_2 \ll P_1$. In terms of the probability amplitudes, this expression becomes

$$g^{(2)}(0) = \frac{2\sum_{m=0}^{\infty}|C_{2,m}|^2}{(\sum_{m=0}^{\infty}|C_{1,m}|^2 + 2\sum_{m=0}^{\infty}|C_{2,m}|^2)^2} \approx \frac{2\sum_{m=0}^{\infty}|C_{2,m}|^2}{(\sum_{m=0}^{\infty}|C_{1,m}|^2)^2}. \tag{A17}$$

Equation (A15) and Equation (A16) show that $C_{1,m} \propto \Omega$ and $C_{2,m} \propto \Omega^2$, respectively. Consequently, $P_1 \propto \Omega^2$ and $P_2 \propto \Omega^4$, which ensures $P_2 \ll P_1$ in the weak-driving regime and justifies the approximation in Equation (A17). By performing Taylor expansion $e^{(\lambda^{(n_2)} - \lambda^{(n_1)})(b^\dagger - b)} \sim 1 + (\lambda^{(n_2)} - \lambda^{(n_1)})(b^\dagger - b)$ on the operator part of Equation (A10) and combining it with Franck Condon factor, we can obtain

$$\langle\tilde{m}(2)|\tilde{l}(1)\rangle_b = \delta_{m,l} - (\lambda^{(n_1)} - \lambda^{(n_2)}\sqrt{l+1})\delta_{m,l+1} + (\lambda^{(n_1)} - \lambda^{(n_2)}\sqrt{l})\delta_{m,l-1}. \tag{A18}$$

According to the above calculation formula, the probability density corresponding to the system can be obtained as

$$\sum_{m=0}^{\infty}|C_{1,m}|^2 \approx \frac{\Omega^2}{(\Delta_c - \delta^{(1)})^2 + \frac{\kappa^2}{4}}, \tag{A19}$$

$$\sum_{m=0}^{\infty}|C_{2,m}|^2 \approx \frac{2\Omega^4}{[(2\Delta_c - \delta^{(2)})^2 + \kappa^2][(\Delta_c - \delta^{(1)})^2 + \frac{\kappa^2}{4}]}, \tag{A20}$$

Finally, by substituting the calculation result of the probability density into Equation (A17), the analytical solution of the second-order correlation function can be obtained:

$$g^{(2)}(0) \approx \frac{2\sum_{m=0}^{\infty}|C_{2,m}|^2}{\sum_{m=0}^{\infty}|C_{1,m}|^4} = \frac{4(\Delta_c - \delta^{(1)})^2 + \kappa^2}{(2\Delta_c - \delta^{(2)})^2 + \kappa^2}. \tag{A21}$$

The explicit driving-strength dependence cancels at the leading order because both P_2 and P_1^2 are proportional to Ω^4. Beyond the weak-driving regime, higher-order corrections and higher-photon-number excitations generally restore the dependence of $g^{(2)}(0)$ on Ω.

Appendix A.3. Derivation of the Cross-Kerr Term in the System Hamiltonian

To clarify the physical origin of the cross-Kerr term, we follow the auxiliary-two-level-system picture used in recent LG-cavity optorotational models, where a two-level system placed on or near the rotating mirror is introduced to mediate an effective cross-Kerr coupling between the cavity field and the rotating mirror. In the present work, the cross-Kerr coupling is not an intrinsic property of the rotating mirror, but is regarded as an effective nonlinear interaction generated by an auxiliary dispersive quantum element. As one possible microscopic route, we consider an auxiliary two-level system or an equivalent atom-like quantum emitter, which is dispersively coupled to the LG cavity mode and its transition frequency is shifted by the rotational mechanical mirror. In the rotating frame of the cavity mode, the auxiliary Hamiltonian may be written as

$$H_{\text{aux}} = (\Delta_e - \eta b^\dagger b)\sigma_+\sigma_- + \hbar g_a(a\sigma_+ + a^\dagger\sigma_-), \tag{A22}$$

where $\Delta_e = \omega_e - \omega_c$ is the detuning between the auxiliary transition and the cavity mode, g_a is the cavity–auxiliary-element coupling strength, and η characterizes the phonon-number-dependent shift of the auxiliary transition. In the large-detuning regime $|\Delta_e - \eta m| \gg g_a\sqrt{n}$, the auxiliary two-level system is only virtually excited and can be adiabatically eliminated. Since the cavity–auxiliary interaction is off-resonant and has no diagonal matrix element in the state, the first-order energy correction vanishes, and the leading dispersive energy shift induced by the virtual transition $|g,n,m\rangle \leftrightarrow |e,n-1,m\rangle$ can be obtained from the second-order perturbation,

$$E^{(2)}_{g,n,m} = \frac{|\langle e,n-1,m|g_a(a\sigma_+ + a^\dagger\sigma_-)|g,n,m\rangle|^2}{E^{(0)}_{g,n,m} - E^{(2)}_{e,n-1,,m}} = -\frac{g_a^2 n}{\Delta_e - \eta m}. \tag{A23}$$

Equivalently, in the operator form,

$$H^{\text{aux}}_{\text{eff}} = -\frac{g_a^2}{\Delta_e - \eta b^\dagger b}a^\dagger a. \tag{A24}$$

For $|\eta m| \ll |\Delta_e|$, this expression can be expanded as

$$H^{\text{aux}}_{\text{eff}} \simeq -\frac{g_a^2}{\Delta_e}a^\dagger a - \frac{g_a^2\eta}{\Delta_e^2}a^\dagger a b^\dagger b. \tag{A25}$$

The first term is an auxiliary-induced Stark shift of the cavity frequency and can be absorbed into the definition of the renormalized ω_c, while the second term gives the effective cross-Kerr interaction

$$H_{\text{ck}} = -g_{\text{ck}} a^\dagger a b^\dagger b, \tag{A26}$$

with $g_{\text{ck}} = \frac{g_a^2\eta}{\Delta_e^2}$. Therefore, the coefficient g_{ck} used in the main text should be understood as an engineered effective nonlinear parameter generated by an auxiliary dispersive element. The validity of this effective description requires large auxiliary detuning and weak auxiliary excitation.

https://doi.org/10.3390/photonics13080725

References

1. Aspelmeyer, M.; Kippenberg, T.J.; Marquardt, F. Cavity optomechanics. *Rev. Mod. Phys.* **2014**, *86*, 1391–1452. [CrossRef]
2. Aspelmeyer, M.; Meystre, P.; Schwab, K. Quantum optomechanics. *Phys. Today* **2012**, *65*, 29–35. [CrossRef]
3. Bose, S.; Jacobs, K.; Knight, P.L. Preparation of nonclassical states in cavities with a moving mirror. *Phys. Rev. A* **1997**, *56*, 4175–4186. [CrossRef]
4. Kippenberg, T.J.; Vahala, K.J. Cavity optomechanics: Back-action at the mesoscale. *Science* **2008**, *321*, 1172–1176. [CrossRef] [PubMed]
5. Walther, H.; Varcoe, B.T.H.; Englert, B.-G.; Becker, T. Cavity quantum electrodynamics. *Rep. Prog. Phys.* **2006**, *69*, 1325–1382. [CrossRef]
6. Ekinci, K.L.; Roukes, M.L. Nanoelectromechanical systems. *Rev. Sci. Instrum.* **2005**, *76*, 061101. [CrossRef]
7. LaHaye, M.D.; Buu, O.; Camarota, B.; Schwab, K.C. Approaching the quantum limit of a nanomechanical resonator. *Science* **2004**, *304*, 74–77. [CrossRef] [PubMed]
8. Teufel, J.D.; Donner, T.; Li, D.; Harlow, J.W.; Allman, M.S.; Cicak, K.; Sirois, A.J.; Whittaker, J.D.; Lehnert, K.W.; Simmonds, R.W. Sideband cooling of micromechanical motion to the quantum ground state. *Nature* **2011**, *475*, 359–363. [CrossRef] [PubMed]
9. Chan, J.; Alegre, T.P.M.; Safavi-Naeini, A.H.; Hill, J.T.; Krause, A.; Gröblacher, S.; Aspelmeyer, M.; Painter, O. Laser cooling of a nanomechanical oscillator into its quantum ground state. *Nature* **2011**, *478*, 89–92. [CrossRef] [PubMed]
10. Ojanen, T.; Børkje, K. Ground-state cooling of mechanical motion in the unresolved sideband regime by use of optomechanically induced transparency. *Phys. Rev. A* **2014**, *90*, 013824. [CrossRef]
11. Liu, Y.; Xiao, Y.; Luan, X.; Wong, C. Optomechanically-induced-transparency cooling of massive mechanical resonators to the quantum ground state. *Sci. China Phys. Mech. Astron.* **2015**, *58*, 1–6. [CrossRef]
12. Vahlbruch, H.; Mehmet, M.; Danzmann, K.; Schnabel, R. Detection of 15 dB squeezed states of light and their application for the absolute calibration of photoelectric quantum efficiency. *Phys. Rev. Lett.* **2016**, *117*, 110801. [CrossRef] [PubMed]
13. Wollman, E.E.; Lei, C.U.; Weinstein, A.J.; Suh, J.; Kronwald, A.; Marquardt, F.; Clerk, A.A.; Schwab, K.C. Quantum squeezing of motion in a mechanical resonator. *Science* **2015**, *349*, 952–955. [CrossRef] [PubMed]
14. Imamoğlu, A.; Schmidt, H.; Woods, G.; Deutsch, M. Strongly interacting photons in a nonlinear cavity. *Phys. Rev. Lett.* **1997**, *79*, 1467–1470. [CrossRef]
15. Curtis, J.B.; Boettcher, I.; Young, J.T.; Maghrebi, M.F.; Carmichael, H.; Gorshkov, A.V.; Foss-Feig, M. Critical theory for the breakdown of photon blockade. *Phys. Rev. Res.* **2021**, *3*, 023062. [CrossRef]
16. Birnbaum, K.M.; Boca, A.; Miller, R.; Boozer, A.D.; Northup, T.E.; Kimble, H.J. Photon blockade in an optical cavity with one trapped atom. *Nature* **2005**, *436*, 87–90. [CrossRef] [PubMed]
17. Neumeier, L.; Leib, M.; Hartmann, M.J. Single-photon transistor in circuit quantum electrodynamics. *Phys. Rev. Lett.* **2013**, *111*, 063601. [CrossRef] [PubMed]
18. Zhou, L.; Yang, L.; Li, Y.; Sun, C.P. Quantum routing of single photons with cyclic three-level system. *Phys. Rev. Lett.* **2013**, *111*, 103604. [CrossRef] [PubMed]
19. Shi, Z.; Chen, X.; Xiang, S. Single-photon router utilizing whispering-gallery resonator coupled with atoms. *Eur. Phys. J. Plus* **2023**, *138*, 568. [CrossRef]
20. Lan, Y.; Li, H.; Zeng, R.; Zhang, X.; Hu, M.; Xu, M.; Zhou, X.; Li, Q. Tunable targeted single-photon routing in a waveguide-QED structure containing a time-modulated two-level atom. *J. Opt. Soc. Am. B* **2024**, *41*, 1395–1402. [CrossRef]
21. Luo, Y.K.; Yang, Y.; Lu, J.; Zhou, L. Control of a single-photon router via an extra cavity. *Appl. Phys. Lett.* **2023**, *123*, 211103. [CrossRef]
22. Baur, S.; Tiarks, D.; Rempe, G.; Dürr, S. Single-photon switch based on Rydberg blockade. *Phys. Rev. Lett.* **2014**, *112*, 073901. [CrossRef] [PubMed]
23. Stannigel, K.; Komar, P.; Habraken, S.J.M.; Bennett, S.D.; Lukin, M.D.; Zoller, P.; Rabl, P. Optomechanical quantum information processing with photons and phonons. *Phys. Rev. Lett.* **2012**, *109*, 013603. [CrossRef] [PubMed]
24. Xiang, Z.; Ashhab, S.; You, J.Q.; Nori, F. Hybrid quantum circuits: Superconducting circuits interacting with other quantum systems. *Rev. Mod. Phys.* **2013**, *85*, 623–653. [CrossRef]
25. Couteau, C.; Barz, S.; Durt, T.; Gerrits, T.; Huwer, J.; Prevedel, R.; Rarity, J.; Shields, A.; Weihs, G. Applications of single photons to quantum communication and computing. *Nat. Rev. Phys.* **2023**, *5*, 326–338. [CrossRef]
26. Rabl, P. Photon blockade effect in optomechanical systems. *Phys. Rev. Lett.* **2011**, *107*, 063601. [CrossRef] [PubMed]
27. Seok, H.; Wright, E.M. Antibunching in an optomechanical oscillator. *Phys. Rev. A* **2017**, *95*, 053844. [CrossRef]
28. Yuan, Z.; Wang, H.; Zhu, A. Controllable photon blockade in double-cavity optomechanical system with Kerr-type nonlinearity. *Quantum Inf. Process.* **2022**, *21*, 22. [CrossRef]
29. Kimble, H.J. The quantum internet. *Nature* **2008**, *453*, 1023–1030. [CrossRef] [PubMed]
30. Radulaski, M.; Fischer, K.A.; Lagoudakis, K.G.; Zhang, J.L.; Vučković, J. Photon blockade in two-emitter-cavity systems. *Phys. Rev. A* **2017**, *96*, 011801. [CrossRef]

31. Miranowicz, A.; Paprzycka, M.; Liu, Y.; Bajer, J.; Nori, F. Two-photon and three-photon blockades in driven nonlinear systems. *Phys. Rev. A* **2013**, *87*, 023809. [CrossRef]
32. Li, Z.; Li, X.; Zhang, G.; Zhong, X. Realizing strong photon blockade at exceptional points in the weak coupling regime. *Front. Phys.* **2023**, *11*, 1168372. [CrossRef]
33. Wang, Y.; Verstraelen, W.; Zhang, B.; Liew, T.C.H.; Chong, Y.D. Giant enhancement of unconventional photon blockade in a dimer chain. *Phys. Rev. Lett.* **2021**, *127*, 240402. [CrossRef] [PubMed]
34. Flayac, H.; Savona, V. Unconventional photon blockade. *Phys. Rev. A* **2017**, *96*, 053810. [CrossRef]
35. Sarma, B.; Sarma, A.K. Quantum-interference-assisted photon blockade in a cavity via parametric interactions. *Phys. Rev. A* **2017**, *96*, 053827. [CrossRef]
36. You, Y.; Feng, L.; Chen, B.; Chen, D.; Peng, Y.; Gong, S. Photon blockade with high photon occupation via cavity electromagnetically induced transparency. *Opt. Express* **2024**, *32*, 17793–17805. [CrossRef] [PubMed]
37. Snijders, H.J.; Frey, J.; Norman, J.C.; Flayac, H.; Savona, V.; Gossard, A.C.; Bowers, J.E.; van Exter, M.P.; Bouwmeester, D.; Löffler, W. Observation of the unconventional photon blockade. *Phys. Rev. Lett.* **2018**, *121*, 043601. [CrossRef] [PubMed]
38. Vaneph, C.; Morvan, A.; Aiello, G.; Féchant, M.; Aprili, M.; Gabelli, J.; Estève, J. Observation of the unconventional photon blockade in the microwave domain. *Phys. Rev. Lett.* **2018**, *121*, 043602. [CrossRef] [PubMed]
39. Turnbull, G.A.; Robertson, D.A.; Smith, G.M.; Allen, L.; Padgett, M.J. The generation of free-space Laguerre-Gaussian modes at millimetre-wave frequencies by use of a spiral phaseplate. *Opt. Commun.* **1996**, *127*, 183–188. [CrossRef]
40. Oemrawsingh, S.S.R.; Eliel, E.R.; Woerdman, J.P.; Verstegen, E.J.K.; Kloosterboer, J.G.; Hooft, G.W. Half-integral spiral phase plates for optical wavelengths. *J. Opt. A Pure Appl. Opt.* **2004**, *6*, S288. [CrossRef]
41. Bhattacharya, M.; Meystre, P. Trapping and cooling a mirror to its quantum ground state. *Phys. Rev. Lett.* **2007**, *99*, 073601. [CrossRef] [PubMed]
42. Bhattacharya, M.; Meystre, P. Using a Laguerre-Gaussian beam to trap and cool the rotational motion of a mirror. *Phys. Rev. Lett.* **2006**, *99*, 153603. [CrossRef] [PubMed]
43. Yao, A.M.; Padgett, M.J. Orbital angular momentum: Origins, behavior and applications. *Adv. Opt. Photonics* **2011**, *3*, 161. [CrossRef]
44. Cao, X.; Huang, S.; Deng, L.; Chen, A. Enhancing the cooling of a rotating mirror in a Laguerre-Gaussian cavity optorotational system via nonlinear cross-Kerr interaction. *Photonics* **2024**, *11*, 960. [CrossRef]
45. Kazemi, S.H.; Mahmoudi, M. Optomechanical second-order sideband effects in a Laguerre-Gaussian rotational cavity system. *Phys. Scr.* **2020**, *95*, 045107. [CrossRef]
46. Xiong, H.; Huang, Y.M.; Wu, Y. Laguerre-Gaussian optical sum-sideband generation via orbital angular momentum exchange. *Phys. Rev. A* **2021**, *103*, 043506. [CrossRef]
47. Peng, J.X.; Chen, Z.; Yuan, Q.Z.; Feng, X.L. Optomechanically induced transparency in a Laguerre-Gaussian rotational-cavity system and its application to the detection of orbital angular momentum of light fields. *Phys. Rev. A* **2019**, *99*, 043817. [CrossRef]
48. Bhattacharya, M.; Giscard, P.L.; Meystre, P. Entanglement of a Laguerre-Gaussian cavity mode with a rotating mirror. *Phys. Rev. A* **2008**, *77*, 013827. [CrossRef]
49. Cheng, H.J.; Zhou, S.J.; Peng, J.X.; Kundu, A.; Li, H.X.; Jin, L.; Feng, X.L. Tripartite entanglement in a Laguerre-Gaussian rotational-cavity system with an yttrium iron garnet sphere. *J. Opt. Soc. Am. B* **2021**, *38*, 285–293. [CrossRef]
50. Chen, Y.; Huang, S.; Deng, L.; Chen, A. Enhanced entanglement of the two cavity modes in the Laguerre-Gaussian cavity optorotating system via an optical parametric amplifier. *Photonics* **2023**, *10*, 926. [CrossRef]
51. Wang, Y.; Zhang, G.Q.; You, W.Y. Photon blockade with cross-Kerr nonlinearity in superconducting circuits. *Laser Phys. Lett.* **2018**, *15*, 105201. [CrossRef]
52. Feng, L.J.; Gong, S.Q. Conventional and unconventional photon blockade with cross-Kerr nonlinearity. *Quantum Inf. Process.* **2022**, *21*, 371. [CrossRef]
53. Solki, H.; Motazedifard, A.; Naderi, M.H. Improving photon blockade, entanglement, and mechanical-cat-state generation in a generalized cross-Kerr optomechanical circuit. *Phys. Rev. A* **2023**, *108*, 063505. [CrossRef]
54. Bayati, S.; Naderi, M.H. Optomechanically induced transparency, absorption, and conversion between slow and fast light in a generalized cross-Kerr optomechanical circuit. *Phys. Lett. A* **2026**, *113*, 013714. [CrossRef]
55. Heikkilä, T.T.; Massel, F.; Tuorila, J.; Khan, R.; Sillanpää, M.A. Enhancing optomechanical coupling via the Josephson effect. *Phys. Rev. Lett.* **2014**, *112*, 203603. [CrossRef]
56. Lai, G.; Huang, S.; Deng, L.; Chen, A. Improving the stationary entanglement of a Laguerre-Gaussian cavity mode with a rotating mirror via nonlinear cross-Kerr interactions and parametric interactions. *Nanomaterials* **2024**, *14*, 1389. [CrossRef] [PubMed]
57. Scully, M.O.; Zubairy, M.S. *Quantum Optics*; Academic Press: Cambridge, UK, 1997.
58. Boyd, R.W. *Nonlinear Optics*, 2nd ed.; Academic Press: San Diego, CA, USA, 2003.
59. Khan, R.; Massel, F.; Heikkilä, T.T. Cross-Kerr nonlinearity in optomechanical systems. *Phys. Rev. A* **2015**, *91*, 043822. [CrossRef]

60. Xiong, W.; Jin, D.Y.; Qiu, Y.; Lam, C.H.; You, J.Q. Cross-Kerr effect on an optomechanical system. *Phys. Rev. A* **2016**, *93*, 023844. [CrossRef]
61. Pirkkalainen, J.M.; Cho, S.U.; Massel, F.; Tuorila, J.; Heikkilä, T.T.; Hakonen, P.J.; Sillanpää, M.A. Cavity optomechanics mediated by a quantum two-level system. *Nat. Commun.* **2015**, *6*, 6981. [CrossRef] [PubMed]
62. Yin, T.S.; Lü, X.Y.; Wan, L.L.; Bin, S.W.; Wu, Y. Enhanced photon-phonon cross-Kerr nonlinearity with two-photon driving. *Opt. Lett.* **2018**, *43*, 2050–2053. [CrossRef] [PubMed]
63. Xie, J.K.; Ma, S.L.; Li, X.K.; Ren, Y.L.; Cao, M.T.; Li, F.L. Exponentially enhanced single-photon cross-Kerr nonlinearity in quantum optomechanics. *Ann. Phys.* **2022**, *534*, 2100599. [CrossRef]
64. Manninen, J.; Haque, M.T.; Vitali, D.; Hakonen, P. Enhancement of the optomechanical coupling and Kerr nonlinearity using the Josephson capacitance of a Cooper-pair box. *Phys. Rev. B* **2022**, *105*, 144508. [CrossRef]
65. Sinclair, J.; Angulo, D.; Lupu-Gladstein, N.; Bonsma-Fisher, K.; Steinberg, A.M. Observation of a large, resonant, cross-Kerr nonlinearity in a cold Rydberg gas. *Phys. Rev. Res.* **2019**, *1*, 033193. [CrossRef]
66. Yang, Z.; Wu, W.; Li, J.; Wang, Y.; You, J. Steady-entangled-state generation via the cross-Kerr effect in a ferrimagnetic crystal. *Phys. Rev. A* **2022**, *106*, 012419. [CrossRef]
67. Lai, G.; Huang, S.; Deng, L.; Chen, A. Enhancing the steady-state entanglement between a Laguerre-Gaussian-cavity mode and a rotating mirror via cross-Kerr nonlinearity. *Photonics* **2023**, *10*, 986. [CrossRef]
68. Shen, Y.; Campbell, G.T.; Hage, B.; Zou, H.; Buchler, B.C.; Lam, P.K. Generation and interferometric analysis of high charge optical vortices. *J. Opt.* **2013**, *15*, 044005. [CrossRef]

https://doi.org/10.3390/photonics13080725